RESEARCH ARTICLE

Strontium isotopes reveal weathering processes in lateritic covers in southern China with implications for paleogeographic reconstructions

Xiao Wei[1,2], **Shijie Wang**[1,3], **Hongbing Ji**[1,4]*, **Zhenhua Shi**[5]

1 State Key Laboratory of Environmental Geochemistry, Institute of Geochemistry, Chinese Academy of Sciences, Guiyang, China, **2** College of Agriculture, Guizhou University, Guiyang, China, **3** Puding Karst Ecosystem Research Station, Chinese Academy of Sciences, Puding, China, **4** Civil and environmental engineering school, University of Science and Technology Beijing, Beijing, China, **5** Guizhou Geological Survey, Guiyang, China

* ji.hongbing@hotmail.com

Abstract

The isotope ratios of Sr are useful tracers for studying parent material sources, weathering processes, and biogeochemical cycling. Mineralogical and geochemical investigations of two lateritic weathering covers, in an area close to the Tropic of Cancer (Guangxi Province, southern China), were undertaken to study the regional weathering processes and Sr isotopic sources. We found that weathering and decomposition of Rb- and Sr-bearing minerals change the Sr isotopic composition in weathering products (lateritic soils). Weathering of illite lowered the $^{87}Sr/^{86}Sr$ ratio whereas dissolving and leaching of carbonate minerals increased the $^{87}Sr/^{86}Sr$ ratio. An Fe nodular horizon is widely developed on the top of the weathering covers in the studied area and it differs from the lateritic soil horizon in mineral composition, construction, and elemental concentration. Furthermore, both Fe_2O_3 and P_2O_5 (concentrations) are negatively correlated with the $^{87}Sr/^{86}Sr$ ratios, suggesting fixation of apatite by Fe oxides is a controlling factor of the Sr isotopic composition in the Fe nodular horizon. The $^{87}Sr/^{86}Sr$ and Nb/Sr ratios imply the contents and proportions of Fe nodules and clay are critical in controlling the changes of Sr isotopic composition in the Fe nodular horizon. The two stages of the weathering process of carbonate rocks are revealed by the $^{87}Sr/^{86}Sr$ versus Nb/Sr diagram. The $^{87}Sr/^{86}Sr$ and Rb/Sr ratios suggest that Sr isotopes in the weathering covers within the studied area are derived mainly from parent rock weathering and that the contributions from allothogenic Sr isotopes are limited. A comparison of Sr isotopic composition signatures in the weathering covers of the studied area and Guizhou Province provided insight into the Sr isotopic source and paleogeographic evolution of southern China. From the Permian to the Triassic, the continental fragment sources of the South China sedimentary basin changed significantly. In the Permian, Southern China presented the paleogeographic pattern that the north was higher (in elevation) than the south.

OPEN ACCESS

Citation: Wei X, Wang S, Ji H, Shi Z (2018) Strontium isotopes reveal weathering processes in lateritic covers in southern China with implications for paleogeographic reconstructions. PLoS ONE 13 (1): e0191780. https://doi.org/10.1371/journal.pone.0191780

Editor: Gregory Carling, Brigham Young University, UNITED STATES

Received: April 15, 2016

Accepted: December 22, 2017

Published: January 26, 2018

Data Availability Statement: All relevant data are within the paper and its Supporting Information files.

Funding: This work was supported by The National Key Basic Research and Development Program (2013CB956702) in http://www.most.gov.cn to Dr. Hongbing JI; The National Natural Science Foundation of China (NSFC) grants (No. 41473122, and 41073096) in: http://www.nsfc.gov.cn to Dr. Hongbing JI; The National Natural Science Foundation of China (NSFC) grants (No.

41473027) in: http://www.nsfc.gov.cn to Dr. XW; The Hundred Talents Program of the Chinese Academy of Sciences in: http://www.cas.cn to Dr. Hongbing Ji; The Orientation Project of Knowledge Innovation Program of the Chinese Academy of Sciences (kzcx2–yw–306) in: http://www.cas.cn to Dr. Shijie Wang.

Competing interests: The authors have declared that no competing interests exist.

Introduction

Weathering is a complex chemical, mechanical, and biological process that operates within various spheres of the land surface system, resulting in the disaggregation of rocks and minerals, pedogenesis, and the formation of weathering covers. The weathering process can change the geomorphologic signature of the land surface [1], control geochemical cycles of various elements [2], and provide nutrients necessary for life [3]. Weathering profiles are considered indicators of internal and external past conditions that may or may not persist. Therefore, studies of the weathering and pedogenesis of rocks and minerals are vital in many fields of geology and geochemistry [4–11].

Sr is an important trace constituent of various rock-forming minerals, and Sr isotopic geochemistry has been used extensively to address a wealth of earth science issues in rock weathering. For example, in natural water bodies, the specific mineral sources of dissolved Sr in catchment waters are studied via the $^{87}Sr/^{86}Sr$ ratio [12–18]. In addition, many attempts have been made to characterize groundwater–rock systems and to trace groundwater pathways in complex hydrogeological settings [19–24]. Recently, Krabbenhöft et al. [25] discussed the Sr isotope equilibrium between inputs and outputs of material during the last glacial maximum (10–30 ka before present) and in modern oceans. Sr isotopes have been used to study material sources of soils and terrestrial deposits [13, 26–27], nutrient cation cycling in ecosystems [28], and significant tectonism [29–30] because it is generally assumed that Sr isotopes are infrequently fractionated by near-surface chemical, physical, and biological processes [31]. However, each mineral is likely to have a distinct $^{87}Sr/^{86}Sr$ ratio [32], and the difference in weathering rates of minerals leads to the variation of Sr isotope composition in weathering products [12,33]. Therefore, Sr isotopes have been used as a tracer for explaining the weathering process [17, 34].

Fe–Mn nodules have strong adsorption capacity for many elements and they are distributed widely in the oceanic floor, lakes, streams, and soils [35–37]. Fe nodules in continental soils generally occur within the tropics, subtropics, Mediterranean climates, and even in temperate regions [37]. Soil Fe nodules are formed within the soil pore space because of seasonal changes in soil redox potential and pH [36, 38–39]. Both the formation and the growth of Fe nodules are also thought associated with bioturbation [40]. Adsorption and coprecipitation of Fe oxides are known to cause enrichment of many trace elements in soil Fe nodules [41]. Consequently, soil Fe nodules play an important role in studies addressing paleoclimate and paleoenvironment evolution, biogeochemical processes, and element enrichment mechanisms in supergene environments [36]. Several studies have published Sr isotopic compositions of Fe-Mn nodules in marine sediments [41–42]. However, current knowledge regarding Sr isotopic compositions of continental soil Fe nodules is limited.

Numerous weathering studies using Sr isotopes have been published; however, most have focused on igneous rocks [32, 43–46], while few have considered carbonate rocks, lateritic soils and soil Fe nodules [47]. In Guangxi Province, the widespread carbonate rocks were covered with thick lateritic soils because of the humid and mild monsoon climate. In the area of southern–central Guangxi Province, plenty of Fe nodules occur within the upper part of lateritic weathering covers, especially in the region around Binyang, Nanning, and Hengxian (Fig 1). Therefore, the natural setting facilitates the study of carbonate rocks, lateritic soils and Fe nodules. In this study, we investigated the Sr isotopic composition signatures of lateritic weathering covers by combining techniques of element geochemistry and mineralogy. The aims of this paper include: (1) the investigation of the mineralogical characteristics and $^{87}Sr/^{86}Sr$ ratio signatures of representative lateritic weathering covers; (2) the determination of mineralogical factors controlling Sr isotopic composition in different stages of rock weathering and

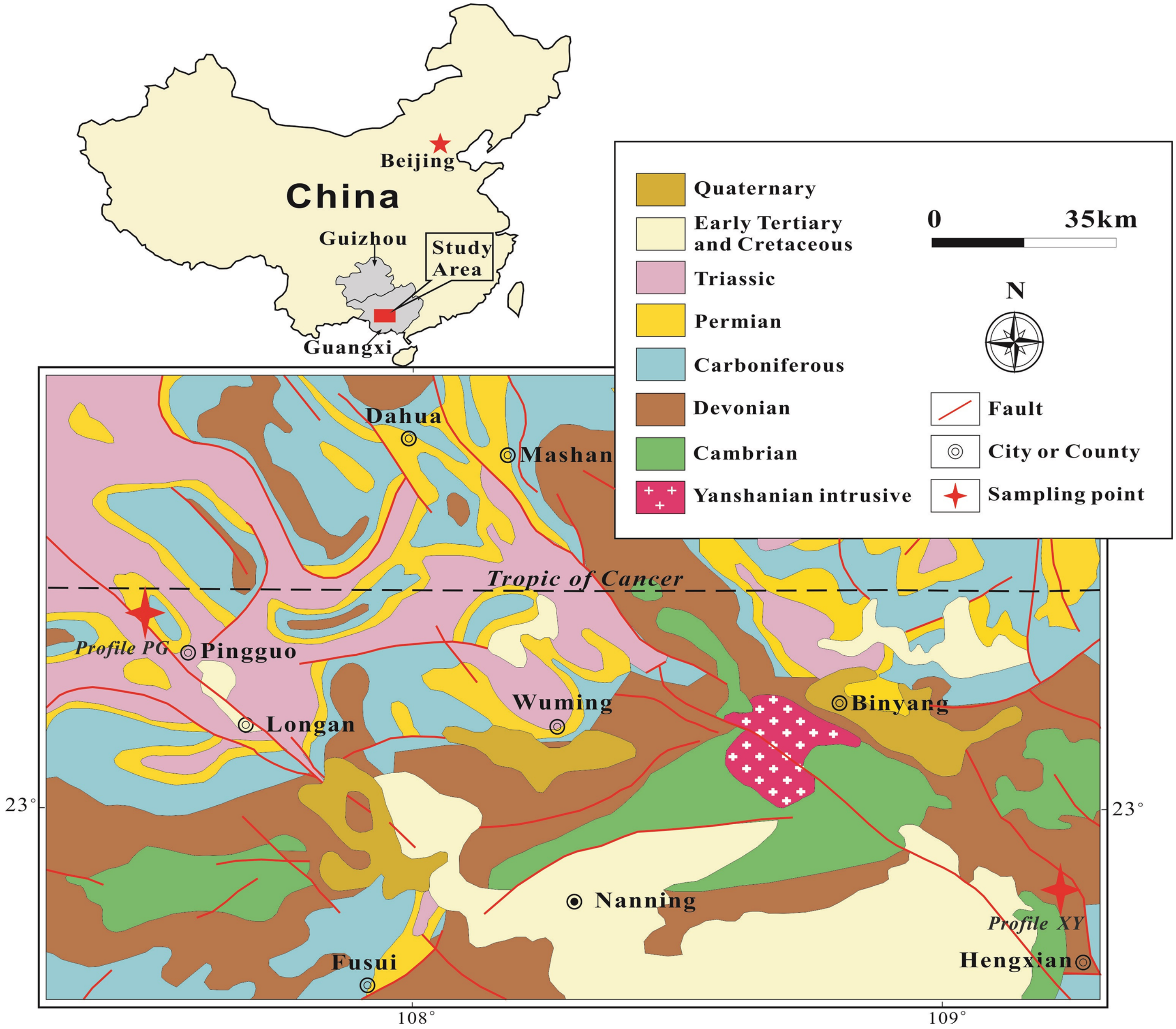

Fig 1. A map of the studied area illustrating locations, sampling sites, stratigraphic and structural characteristics.

https://doi.org/10.1371/journal.pone.0191780.g001

pedogenesis; (3) the examination of the significance of $^{87}Sr/^{86}Sr$ ratio for evaluating weathering and pedogenesis processes of carbonate rocks; and (4) the evaluation of terrigenous Sr isotopic sources in the South China deposition basin during the Late Paleozoic.

Setting

Geomorphology and climate

Guangxi Province, located in southern China (Fig 1), has a mean elevation of 800 m and a wide range of geomorphic environments. The studied area is situated in the middle of Guangxi Province and it has a mean elevation of 50 m. The landforms are primarily karst plains and low hills that contrast with the mountainous region to the northwest and coastal plains to the south. The gentle terrain and hot and humid climate have promoted the formation and development of thick lateritic weathering covers. There is typically a loose Fe nodular horizon in the upper part of the weathering cover within this region, which is similar to the lateritic profiles in the equatorial zone described by Braun et al. [48].

The studied area lies near the Tropic of Cancer where the hot and humid tropical monsoon climate [49] and the alternation of wet (April–September) and dry (October–March) seasons are beneficial to the formation of Fe nodules [50]. The average annual temperature and average annual rainfall of the entire province are 21.5 ± 5˚C and 1580 ± 300 mm/a, respectively. Evergreen broadleaf forest is the primary vegetation type within the studied area, which limits water and soil losses and induces strong evapotranspiration.

Regional geology

Guangxi Province lies on the southern fringe of the Yangtze continental block. Multi-period and intensive tectonic movements have resulted in an outcrop pattern that includes various strata of differing ages (Fig 1). The oldest exposed strata in the studied area are Cambrian shale and sandstone. Between the Cambrian strata and overlying Devonian rocks, there is an angular unconformity, along which Ordovician and Silurian strata have been removed.

Devonian and Carboniferous rocks, distributed extensively within the studied area, are dominated by carbonate lithologies. Permian and Triassic successions are also dominated by carbonate rocks and they are in conformable contact with the underlying Carboniferous strata. The Yanshanian igneous body, formed during the Jurassic to Early Cretaceous, is exposed near Binyang County within the province and it comprises mainly biotite adamellite [49]. The Cretaceous and early Tertiary succession is dominated by red sandstone, separated from older rocks by another angular unconformity.

Materials and methods

Ethics statement

We state that no specific permissions were required for these locations/activities because the field work was not carried out on private land. Furthermore, in China, normal science studies are licensed and protected by the state.

Sampling

To study the weathering and pedogenesis processes of carbonate rocks, as well as the formation and evolution mechanisms of Fe nodules within the tropics, two representative lateritic soil profiles in Guangxi Province were investigated. Profile XY is located in northern Hengxian County (22˚51′6.6″N, 109˚14′12.2″E) where the outcrops are mainly Devonian argillaceous limestone and calcareous shale. Profile PG is situated in western Pingguo County (23˚24′20.5″N, 107˚29′57.1″E), where the bedrock is Permian limestone (Fig 1). The different bedrock lithologies are responsible for the differences in mineralogical compositions and geochemical characteristics between profiles XY and PG.

Based on profile characteristics such as the structure, physical property, mineralogy, geochemistry, and weathering intensity, profile XY can be divided into two layers: an Fe nodular horizon and a mottled clay layer (Fig 2). The Fe nodular horizon contains abundant Fe nodules (sizes: 0.5–10.0 cm) distributed loosely within the lateritic soil. The large nodules (>1 cm) are composed of smaller nodules cemented by Fe oxides/hydroxides. Generally, the quantities and grain sizes of Fe nodules decrease with depth. The mottled clay layer consists of

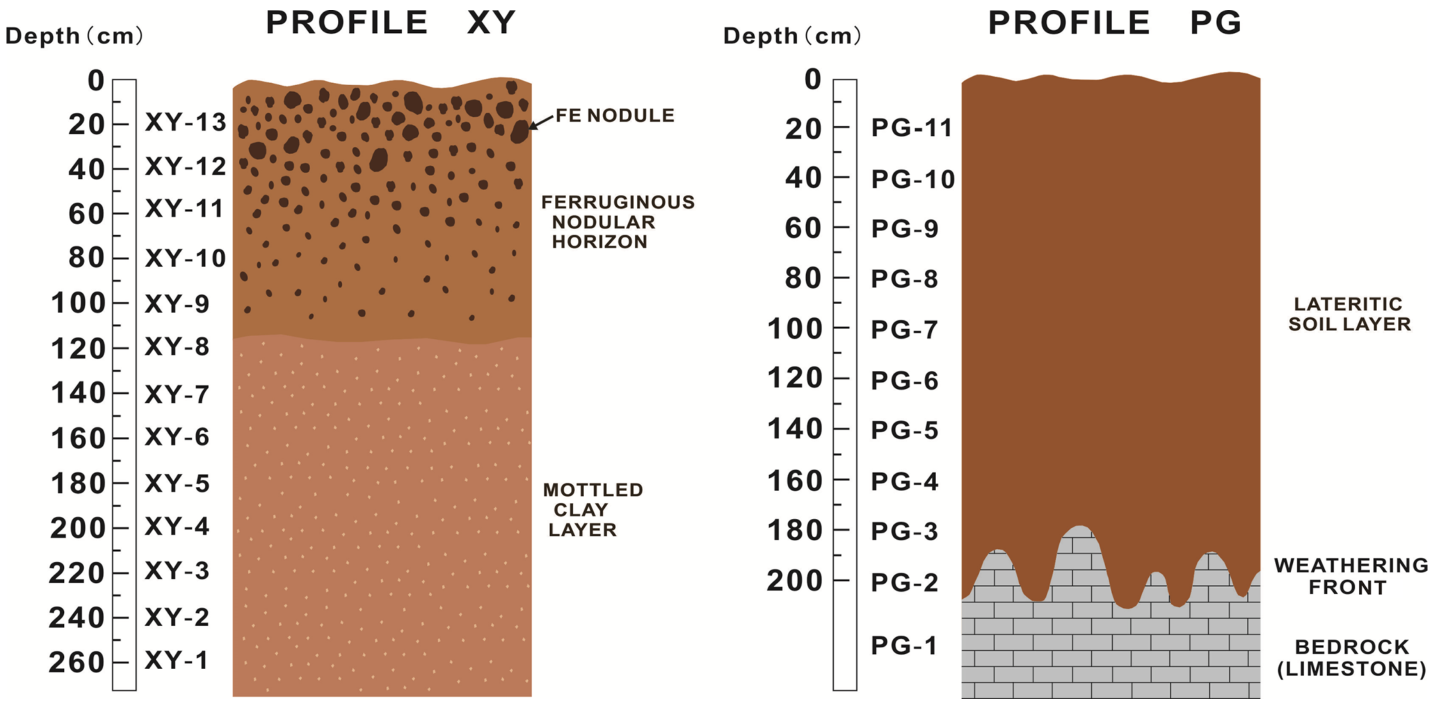

Fig 2. Schematic representation of studied weathering profiles showing the sectional structure and sampling depth.

https://doi.org/10.1371/journal.pone.0191780.g002

intermixed red and yellow clay. The profile was too thick to reach the bedrock and weathering front; however, the bedrock was assumed similar to the general geology within this area, i.e., Devonian argillaceous limestone. In contrast, profile PG is composed of homogeneous lateritic soil without obvious colored layering. The profile was created by excavators and the total thickness is about 2 m. The bedrock is the Permian Maokou Formation limestone and the weathering front is undulating.

Before sampling, the surface soil of each weathering profile (about 5–10 cm) was removed. Channel sampling was adopted to collect samples from bottom to top and each sample interval was 20 cm. The detailed sampling method follows [51]. Samples were collected and placed into sample sacks and transported to the laboratory within one week, where they were air dried for three weeks in the opened bags before processing.

Analysis methods

The air-dried rock and soil samples used for the whole-rock geochemical analyses were ground in an agate mortar and sieved trough a 200 mesh (74 μm) light sieve.

X-ray diffraction (XRD) was used to determine the mineral composition, and the semi-quantitative calculation of the mineral phase was based on the lamellae spacing (d value) and X-ray relative intensity (I/I_1). The experimental apparatus was a D/max–2000 model XRD diffractometer, including the instrument standard Cu Kα target, with settings of 40 Kv, 20 mA, and scanning scope for 2–60˚.

For X-ray fluorescence (XRF) spectrometric analysis of the major elements, the powdered sample was mixed with lithium tetraborate flux and melted in a platinum crucible at a temperature of 1100˚C. The fused samples were cooled into glass wafers and used for major element content testing using a Philips PW 2402 XRF spectrometer. The standard test errors for all major elements were <5%.

The CIA (chemical index of alteration) was used to evaluate the weathering extent quantitatively. CIA = $Al_2O_3/(Al_2O_3 + CaO^* + Na_2O + K_2O) \times 100$ [52], where oxide contents refer to molar contents and CaO^* represents the CaO content in the silicate fraction of the test sample. The CaO contents in carbonate (calcite and dolomite) and phosphate (apatite) minerals are normally accomplished, calculated, and corrected by measured CO_2 and P_2O_5 contents. The CaO^* content is a corrected value, which is approximately equal to the surplus of the CaO content in the whole test samples minus the CaO content in the carbonate and phosphate minerals [53–54].

For trace element and Sr isotope analyses, powdered test samples were digested with a mixture of concentrated nitric and hydrofluoric acid (twice-distilled purification) in Teflon® high–pressure digestion tanks at a temperature of 190˚C for more than 48 h. The dissolved samples were split into two parts: one for trace element concentration analysis and the other for Sr isotopic composition testing. The trace element contents of the samples were measured by Inductively Coupled Plasma Mass Spectroscopy (ICP–MS) (Element I, Finnigan MAT Company) with Rh as the internal standard. The split for the Sr isotope testing was transformed into a hydrochloric acid medium by drying the distillate and adding hydrochloric acid (1.8–2.0 mol/L), repeatedly. The prepared solution was penetrated through cation exchange columns (AG50WX8, 200–400 mesh resin) to separate Sr from other ions. During the lessivation, 1.8–2.0 mol/L hydrochloric acid was used as an elution acid. Isotopic measurements were then performed by multicollector Thermal Ionization Mass Spectrometry (TIMS) (IsoProbe–T, U.K. GV Company). TIMS typically provides a value of the $^{87}Sr/^{86}Sr$ ratio of 0.710235 ± 0.000014 (2σ, n = 26) for the NBS987 Sr standard, and the measured isotope data are precise to 0.003% or better.

The major and trace element data of all samples were provided by the Beijing Research Institute of Uranium Geology, and the mineral and Sr isotopic composition testing was completed at the state Key Laboratory of Environmental Geochemistry, Institute of Geochemistry, Chinese Academy of Sciences.

In order to determine the bulk densities of the soils, the paraffin-coated clod method was used [55]. The pH values of the earth samples were determined with a pH meter. The solid-to-liquid ratio was 2.5:1.0, and the soak solution was ultra-pure water.

Results

Mineralogical composition

In profile XY, the main minerals identified by XRD in the Fe nodular horizon (represented by sample XY–11) are iron oxide minerals (such as goethite and hematite), clay minerals (mainly kaolinite and small amounts of illite), and gibbsite (Fig 3). In the mottled clay layer (XY–1 and XY–7), the main minerals are illite and quartz with small amounts of smectite, calcite, plagioclase, and orthoclase. From the mottled clay layer to the Fe nodular horizon, the concentrations of illite and plagioclase decrease with increasing contents of kaolinite and iron oxides. In comparison, profile PG is characterized by high contents of kaolinite and gibbsite and low content of illite. The mineralogical compositions and concentrations in the samples of profile PG do not show particular variation, except the calcite content is higher in sample PG–2.

Chemical composition

The selected major and trace element concentrations, CIA values, and $^{87}Sr/^{86}Sr$ ratios of the bulk samples are listed in Tables 1 and 2, and the variation of several selected element concentrations and other geochemical parameters in the vertical direction are plotted in Fig 4. Because of the dilution effect of $CaCO_3$, various elements in the bedrock sample (PG–1) of profile PG show very low contents but Sr remains relatively high. Concentrations of multiple

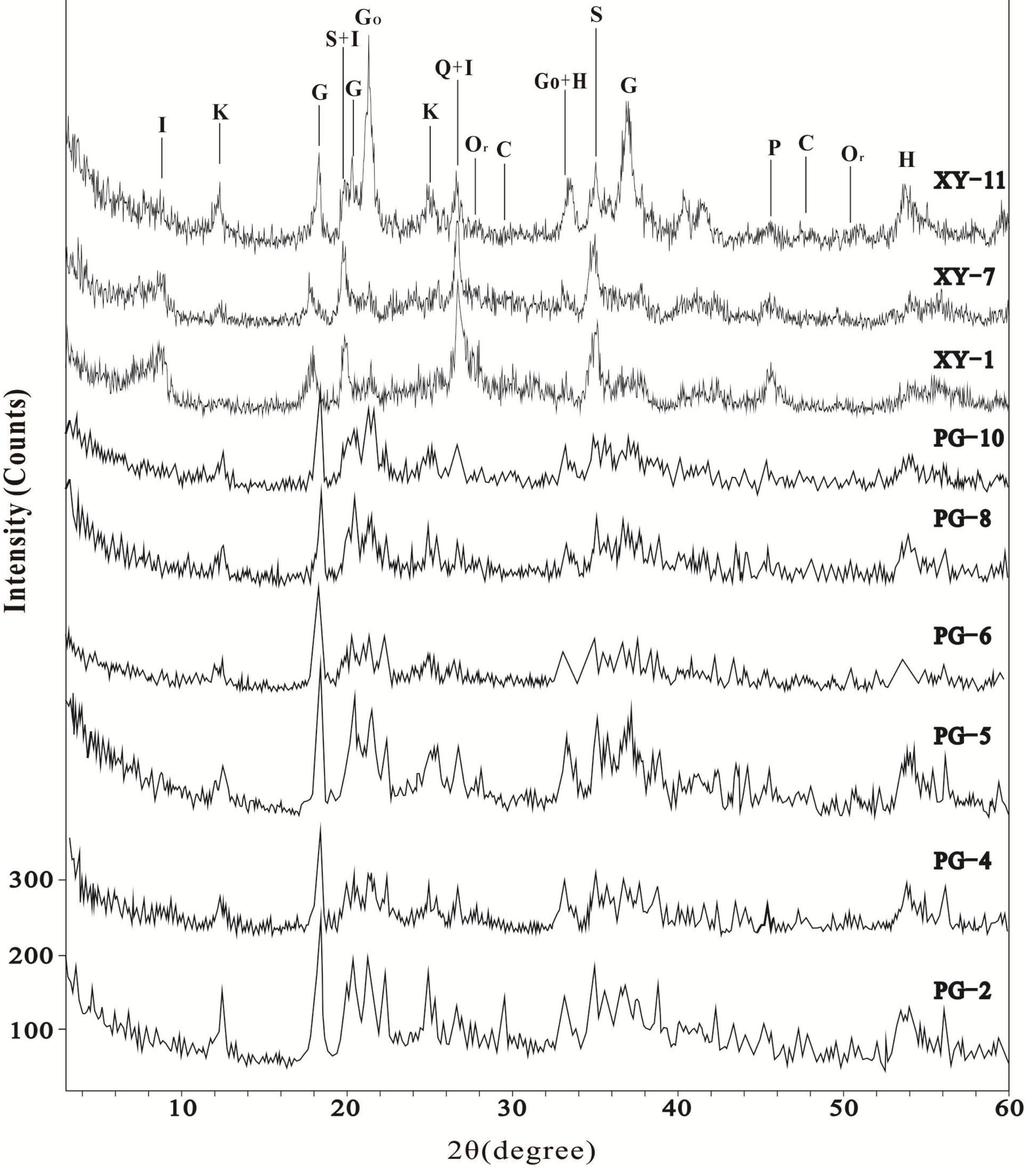

Fig 3. XRD patterns of selected Fe nodule and soil samples from profiles XY and PG. G–gibbsite, Go–goethite, H–hematite, I–illite, K–kaolinite, Or–orthoclase, P–pyrophyllite, Q–quartz, S–smectite, C–calcite.

https://doi.org/10.1371/journal.pone.0191780.g003

major elements in profile PG have no significant changes with depth, whereas concentrations of several trace elements (Sr, Th, and U) show significant fluctuation. P_2O_5, Sr, Th, and U

Table 1. Selected major and trace element concentrations, $^{87}Sr/^{86}Sr$ ratios and physicochemical parameters of bulk samples of weathering profile XY in the study area.

Profile	PROFILE XY												
Sample	**XY–1**	**XY–2**	**XY–3**	**XY–4**	**XY–5**	**XY–6**	**XY–7**	**XY–8**	**XY–9**	**XY–10**	**XY–11**	**XY–12**	**XY–13**
Petrography	M ^{a}	M ^{a}	M ^{a}	M ^{a}	M ^{a}	M ^{a}	M ^{a}	M ^{a}	F ^{a}	F ^{a}	F ^{a}	F ^{a}	F ^{a}
Bulk density (g/cm^{-3})	1.55	1.39	1.49	1.48	1.47	1.43	1.59	1.25	2.27 ^{b}	2.03 ^{b}	2.14 ^{b}	2.26 ^{b}	2.13 ^{b}
pH	4.48	4.49	4.49	4.46	4.45	4.44	4.42	4.24	4.23 ^{c}	4.38 ^{c}	4.48 ^{c}	4.61 ^{c}	4.64 ^{c}
CIA	77.23	78.49	77.73	79.35	79.33	78.87	79.34	82.08	89.00	92.79	94.23	96.06	95.63
SiO_2/%	46.37	46.37	45.31	45.03	42.36	43.72	44.09	39.53	33.94	26.47	22.69	17.59	13.60
Al_2O_3/%	24.86	25.58	24.60	24.99	22.05	23.47	24.47	24.15	26.21	23.62	21.86	21.78	15.41
Fe_2O_3/%	10.02	9.44	10.97	11.00	17.50	14.36	12.49	17.39	19.49	28.44	35.13	39.96	50.36
CaO/%	0.06	0.06	0.09	0.07	0.06	0.07	0.08	0.05	0.11	0.11	0.12	0.10	0.08
P_2O_5/%	0.05	0.03	0.03	0.04	0.04	0.04	0.06	0.04	0.07	0.09	0.11	0.12	0.12
Na_2O/%	0.16	0.15	0.16	0.15	0.13	0.15	0.15	0.12	0.12	0.096	0.084	0.076	0.066
K_2O/%	6.53	6.25	6.27	5.78	5.11	5.58	5.66	4.69	2.81	1.55	1.11	0.71	0.55
Rb/$\times 10^{-6}$	213.00	136.00	222.00	214.00	196.00	228.00	215.00	155.00	98.90	69.90	55.30	38.50	33.90
Sr/$\times 10^{-6}$	21.30	14.70	23.30	26.10	24.30	33.10	35.70	28.80	33.90	33.10	31.00	36.70	33.60
Rb/Sr	10.00	9.25	9.53	8.20	8.07	6.89	6.02	5.38	2.92	2.11	1.78	1.05	1.01
Nb/$\times 10^{-6}$	16.70	16.30	17.10	19.00	16.60	18.10	21.40	21.60	27.90	30.80	29.80	37.20	34.90
Nb /Sr	0.78	1.11	0.73	0.73	0.68	0.55	0.60	0.75	0.82	0.93	0.96	1.01	1.04
$^{87}Sr/^{86}Sr$	0.878079	0.853491	0.867591	0.833849	0.825195	0.843111	0.807383	0.806676	0.752441	0.738346	0.732884	0.724301	0.723564

Note

a M, F refer to mottled clay layer and Fe nodular horizon, respectively.

b They are the bulk density of Fe nodules.

c They are the pH value of soils which surround the Fe nodules.

https://doi.org/10.1371/journal.pone.0191780.t001

display obvious depleted contents in lateritic soil samples PG–5, PG–9, and PG–10. Concentrations of Fe_2O_3, P_2O_5, Sr, Th, and U in profile XY decrease with depth, and in the Fe nodular horizon, these elements are more enriched than in the soil layers. However, concentrations of other oxides (SiO_2, Al_2O_3, Na_2O, and K_2O) show the opposite trend (Fig 4), which is interpreted as the dilution effect of iron [50].

The rare earth element (REE) contents and relevant parameters are listed in Tables 3 and 4, and PAAS (Post-Archean Australian Shale) normalized REE distribution patterns [56] are shown in Fig 5. In profile XY, the test data show that the total REE content (ΣREE) in the nodules (366.57–696.08 ppm) is higher than in the mottled clay (162.86–296.28 ppm, except in sample XY–7: 445.81 ppm). The obvious REE fractionations between the Fe nodular horizon and mottled clay layer are observed in Fig 5. Compared with the mottled clay, the Fe nodules show enrichment of middle and heavy REEs (MREEs and HREEs, respectively) and loss of light REEs (LREEs). Ce anomalies in the whole profile are not obvious (δCe rangs from 0.89 to 1.01). The REEs in sample XY–7 yield evident fractionations. The higher ΣREE and LREE contents indicate that this horizon is the zone of REE enrichment. In profile PG, compared with the bed rock (PG-1) (ΣREE is 1.07), soils presents significant REE concentration (ΣREE ranges from 296.06 to 759.81 ppm). Sample PG-1 shows obvious negative Ce anomaly (δCe is 0.68), whereas soil samples have no distinct Ce anomalies (δCe rangs from 0.87to 1.27), except PG-10 (δCe is 1.63). Samples PG–5, PG–9, and PG–10 have depleted ΣREE (491.14, 483.05, and 296.06 ppm) compared with the other lateritic soil samples (528.48–759.81 ppm). In addition, samples PG–5, PG–9, and PG–10 show distinct depleted MREEs and HREEs in Fig 5.

Table 2. Selected major and trace element concentrations, 87Sr/86Sr ratios and physicochemical parameters of bulk samples of weathering profile PG in the study area.

Profile						PROFILE PG					
Sample	**PG–1**	**PG–2**	**PG–3**	**PG–4**	**PG–5**	**PG–6**	**PG–7**	**PG–8**	**PG–9**	**PG–10**	**PG–11**
Petrography	L[a]	S[a]	S[a]	S[a]	S[a]	S[a]	S[a]	S[a]	S[a]	S[a]	S[a]
Bulk density (g/cm^{-3})	2.67	1.64	1.57	1.55	1.51	1.61	1.50	1.53	1.45	1.49	1.26
pH	—[b]	7.79	7.03	7.05	6.95	7.04	7.01	6.89	7.15	7.23	7.28
CIA	—	96.21	96.35	96.31	96.41	96.48	96.32	96.24	96.01	95.85	96.30
SiO_2/%	0.70	24.04	24.21	24.21	24.20	24.30	24.85	24.90	25.17	25.93	24.99
Al_2O_3/%	0.54	31.80	31.89	31.89	32.51	32.37	31.90	31.53	31.20	31.19	31.30
Fe_2O_3/%	0.16	19.40	20.71	20.80	20.30	20.36	20.30	20.32	19.91	19.80	20.32
CaO/%	52.61	1.74	0.48	0.44	0.37	0.36	0.37	0.42	0.57	0.49	0.43
P_2O_5/%	0.01	0.13	0.14	0.15	0.15	0.15	0.15	0.16	0.14	0.14	0.16
Na_2O/%	0.063	0.13	0.13	0.13	0.13	0.12	0.13	0.13	0.13	0.13	0.12
K_2O/%	0.02	0.96	0.92	0.93	0.92	0.91	0.93	0.94	1.00	1.05	0.93
Rb/$\times10^{-6}$	—	81.20	77.20	91.40	66.00	86.30	79.30	88.80	76.20	27.00	85.20
Sr/$\times10^{-6}$	95.80	166.00	127.00	151.00	66.20	153.00	118.00	143.00	79.50	44.10	125.00
Rb/Sr	—	0.49	0.61	0.61	1.00	0.56	0.67	0.62	0.96	0.61	0.68
Nb/$\times10^{-6}$	0.05	58.60	63.60	73.70	71.00	73.60	61.70	58.60	53.50	52.70	51.50
Nb /Sr	0.00	0.35	0.50	0.49	1.07	0.48	0.52	0.41	0.67	1.20	0.41
$^{87}Sr/^{86}Sr$	0.707991	0.710465	—	0.711050	0.711050	0.711030	0.711052	0.711103	—	0.711059	0.711279

Note

a L and S refer to limestone and lateritic soil samples, respectively.

b—represents unanalyzed data or the content below the detection limit.

https://doi.org/10.1371/journal.pone.0191780.t002

Sr isotope signature and CIA (chemical index of alteration)

The variations in range of CIA values and $^{87}Sr/^{86}Sr$ and Rb/Sr ratios in the samples of profile XY are larger (CIA = 77.23–96.06, $^{87}Sr/^{86}Sr$ = 0.723564–0.878079, Rb/Sr = 1.01–10.00). By contrast, those parameters in the samples of profile PG do not change significantly (CIA = 95.85–96.48, $^{87}Sr/^{86}Sr$ = 0.710465–0.711279, Rb/Sr = 0.49–0.95) (Tables 1 and 2). In comparison with profile PG, profile XY has higher $^{87}Sr/^{86}Sr$ and Rb/Sr ratios and lower CIA values (Fig 4).

The CIA values of profile XY decrease with depth (Fig 4). In addition, samples in the Fe nodular horizon (depth: 100 cm) of profile XY show a higher degree of weathering than the mottled clay layer (below 120 cm). The CIA values of profiles PG are higher and there are no significant changes in CIA as the sampling depth increases. The $^{87}Sr/^{86}Sr$ and Rb/Sr ratios of profile XY increase downward. The $^{87}Sr/^{86}Sr$ ratios in profile PG are nearly constant, although the Rb/Sr ratios of samples at 60 and 140 cm in profile PG have a slight increase.

Discussion

Changes of Sr isotopic composition in weathering covers

Sr isotopes are infrequently fractionated by near-surface chemical, physical, and biological processes [31]. However, weathering and decomposition of specific Sr-bearing minerals could lead to the modification of the Sr isotopic composition [32, 57–62]. The $^{87}Sr/^{86}Sr$ ratios of profile XY decrease upwards with the intensification of weathering, while those of profile PG remain nearly constant (Fig 4). The reasons and controlling factors for the changes in the Sr isotopic composition of the two profiles are discussed below.

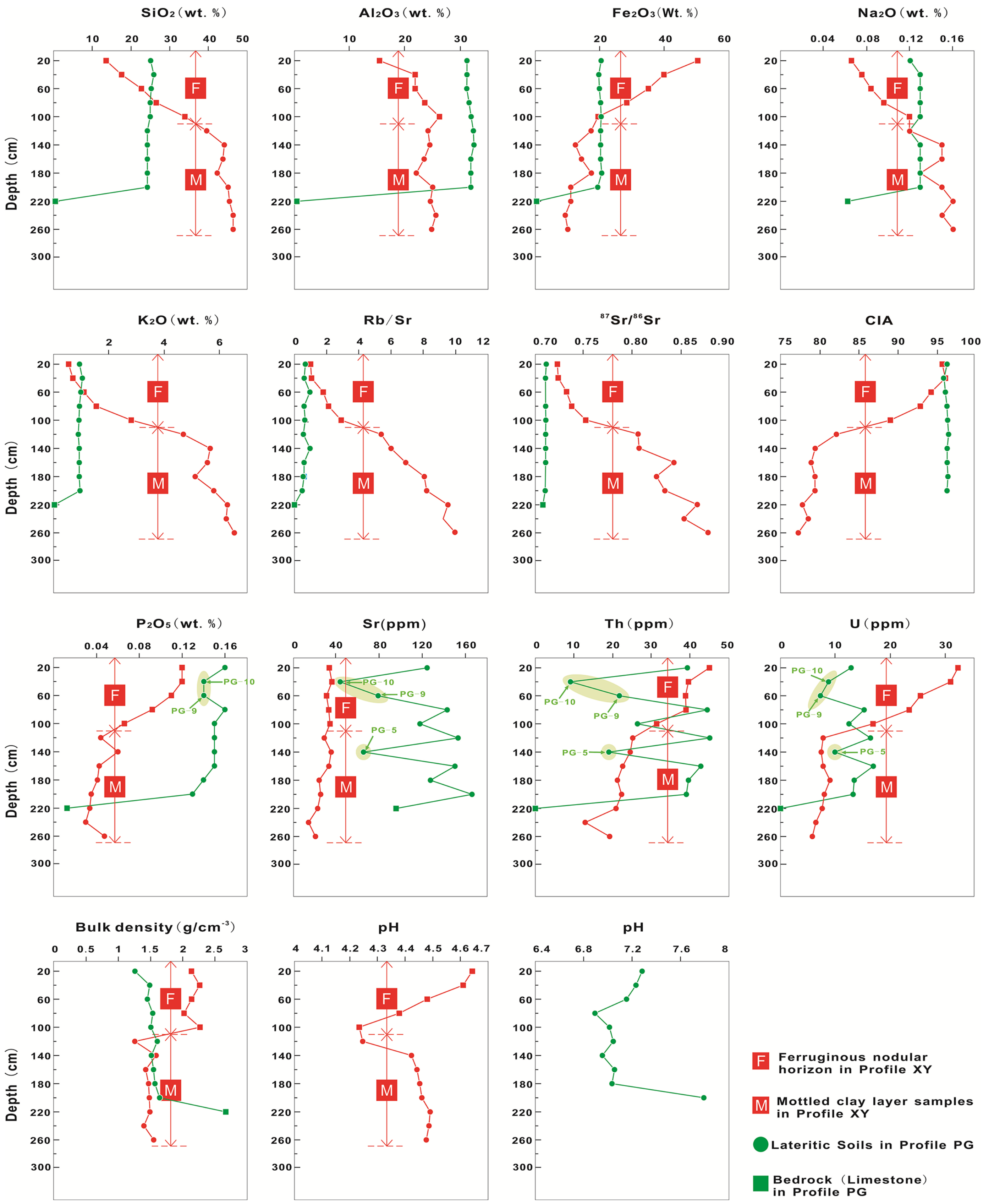
SiO₂ (wt. %)
Al₂O₃ (wt. %)
Fe₂O₃ (Wt. %)
Na₂O (wt. %)
K₂O (wt. %)
Rb/Sr
⁸⁷Sr/⁸⁶Sr
CIA
P₂O₅ (wt. %)
Sr (ppm)
Th (ppm)
U (ppm)
Bulk density (g/cm⁻³)
pH
pH
Depth (cm)
20
60
100
140
180
220
260
300
F
M
PG-10
PG-9
PG-5
F Ferruginous nodular horizon in Profile XY
M Mottled clay layer samples in Profile XY
Lateritic Soils in Profile PG
Bedrock (Limestone) in Profile PG

Fig 4. Distributions of selected major elements and changes of several relevant physicochemical parameters along with the vertical sampling depth.

https://doi.org/10.1371/journal.pone.0191780.g004

XRD data show that from the bottom to top of profile XY, illite decreases as kaolinite increases. It indicates that illite is weathered and transformed into kaolinite with increasing weathering intensity (Fig 3). Meanwhile, XRD data also indicate the main K-bearing mineral in profile XY is illite (Fig 3). Therefore, the upward decrease of K_2O concentrations in profile XY also confirms the weathering and decomposition of illite (Fig 4). In addition, the $^{87}Sr/^{86}Sr$ ratios show obvious positive correlations with K_2O concentrations ($R^2 = 0.98$ in the Fe nodular horizon and $R^2 = 0.73$ in the mottled clay layer) and negative correlations with CIA value ($R^2 = 0.99$ in the Fe nodular horizon and $R^2 = 0.74$ in the mottled clay layer) in profile XY (Fig 6A and 6B). It suggests a strong link between the weathering and decomposition of illite and changes of the $^{87}Sr/^{86}Sr$ ratios in profile XY.

K-bearing minerals usually contain abundant Rb because of the similar ionic radii and equal electrovalence of K and Rb. Accordingly, the $^{87}Sr/^{86}Sr$ ratios in K-bearing minerals such as biotite, K-feldspar, and illite are usually very high because ^{87}Sr is derived from ^{87}Rb by beta decay. Therefore, decomposition of K-bearing minerals in rocks might lead to decreased $^{87}Sr/^{86}Sr$ ratios in the residual weathering products relative to their parent rocks. [61, 63–65]. In summary, the appearance of illite in profile XY is the key factor behind the higher $^{87}Sr/^{86}Sr$ ratios in the weathering cover. Furthermore, the weathering and decomposition of illite is a critical controlling factor for $^{87}Sr/^{86}Sr$ ratios. However, compared with profile XY, the samples in profile PG have lower K_2O concentrations and no significant correlation between K_2O concentrations and $^{87}Sr/^{86}Sr$ ratios (Figs 4 and 6A).

Liu et al. [62] have done a leaching experiment of limestone in Guizhou province. The result shows that Sr isotopes in carbonate rock have two distinct sources: one part derives

Table 3. Rare earth element concentrations and relevant parameters of bulk samples in weathering profiles XY in the study area.

Profile	**PROFILE XY**												
Sample	**XY–1**	**XY–2**	**XY–3**	**XY–4**	**XY–5**	**XY–6**	**XY–7**	**XY–8**	**XY–9**	**XY–10**	**XY–11**	**XY–12**	**XY–13**
La	42.00	31.50	53.10	65.40	50.80	67.20	98.60	46.70	63.40	74.90	69.10	73.40	72.80
Ce	94.40	82.70	111.00	122.00	105.00	129.00	173.00	87.40	202.00	389.00	239.00	466.00	241.00
Pr	10.20	7.25	12.10	13.00	10.40	13.50	26.50	10.00	12.80	16.90	15.80	16.20	17.50
Nd	38.80	28.20	46.10	47.20	39.20	52.10	97.9	37.70	45.60	60.50	58.90	64.90	69.30
Sm	6.35	4.94	9.11	7.53	7.20	8.22	15.70	6.37	8.25	12.00	11.90	13.30	15.20
Eu	1.34	0.97	1.84	1.47	1.43	1.51	2.65	1.18	1.70	2.45	2.60	2.83	2.92
Gd	6.11	4.47	9.03	6.77	6.91	7.25	10.80	4.91	8.25	12.90	12.50	14.90	15.80
Tb	1.01	0.767	1.63	1.12	1.15	1.08	1.59	0.86	1.39	2.21	2.33	2.66	2.94
Dy	6.39	4.52	9.52	6.79	6.64	6.52	7.93	4.76	8.73	13.10	14.70	16.20	18.50
Ho	1.27	0.88	1.78	1.27	1.32	1.09	1.38	1.00	1.79	2.66	2.97	3.39	3.83
Er	3.75	2.79	5.41	3.98	3.87	3.82	4.27	3.21	5.47	8.08	9.19	10.00	11.00
Tm	0.56	0.47	0.89	0.69	0.65	0.55	0.67	0.58	0.86	1.21	1.34	1.57	1.75
Yb	4.01	2.97	5.46	3.97	4.02	3.87	4.18	3.43	5.50	7.56	7.86	9.27	11.00
Lu	0.60	0.44	0.82	0.67	0.63	0.58	0.64	0.56	0.83	1.18	1.30	1.46	1.61
δEu[a]	1.05	1.11	1.01	0.97	1.05	0.99	0.78	0.93	1.64	2.52	1.67	3.12	1.56
δCe[a]	1.01	0.97	0.96	0.97	0.95	0.92	0.96	0.99	0.97	0.93	1.00	0.95	0.89
ΣREE	216.79	162.86	267.79	281.86	239.22	296.28	445.81	208.66	366.57	604.65	449.49	696.08	485.15

Note

a represent PAAS (Post–Archean Australian Shale) normalized values [56].

https://doi.org/10.1371/journal.pone.0191780.t003

Table 4. **Rare earth element concentrations and relevant parameters of bulk samples in weathering profiles PG in the study area.**

Profile						PROFILE PG					
Sample	**PG–1**	**PG–2**	**PG–3**	**PG–4**	**PG–5**	**PG–6**	**PG–7**	**PG–8**	**PG–9**	**PG–10**	**PG–11**
La	0.29	121.00	116.00	135.00	95.30	110.00	94.80	109.00	99.40	45.50	103.00
Ce	0.37	254.00	244.00	295.00	205.00	284.00	232.00	258.00	184.00	156.00	235.00
Pr	0.06	29.30	28.80	34.20	21.80	24.20	21.10	25.40	23.80	10.70	22.10
Nd	0.19	116.00	122.00	140.00	87.00	92.70	84.50	97.30	96.00	41.50	84.50
Sm	0.02	25.60	27.80	32.80	19.20	22.60	19.10	24.20	19.10	8.67	19.10
Eu	0.01	4.87	5.37	6.40	3.37	4.34	3.76	4.70	3.64	1.81	3.74
Gd	0.03	23.00	24.70	27.90	14.90	19.00	16.70	20.80	16.70	8.35	17.00
Tb	0.01	4.19	4.69	5.47	2.91	4.08	3.35	4.00	2.71	1.48	3.13
Dy	0.04	24.60	26.60	31.50	16.40	24.10	19.60	23.00	15.10	8.35	18.60
Ho	0.01	4.67	5.43	6.13	2.93	4.75	3.70	4.60	2.88	1.64	3.58
Er	0.03	14.80	15.90	18.70	8.87	15.20	11.70	14.60	8.31	4.96	11.30
Tm	0.01	2.60	2.76	3.23	1.54	2.81	2.08	2.53	1.39	0.85	2.02
Yb	0.03	16.00	16.80	20.30	10.40	18.50	14.10	16.00	8.70	5.48	12.70
Lu	—^{b}	2.59	2.64	3.18	1.52	2.74	1.99	2.31	1.32	0.77	1.88
δEu^{a}	1.39	0.95	0.96	1.00	0.94	0.99	0.99	0.99	0.96	1.00	0.98
δCe^{a}	0.68	0.98	0.97	1.00	1.04	1.27	1.20	1.13	0.87	1.63	1.14
ΣREE	1.07	643.22	643.49	759.81	491.14	629.02	528.48	606.44	483.05	296.06	537.65

Note

a represent PAAS (Post–Archean Australian Shale) normalized values [56].

b—represents unanalyzed data or the content below the detection limit.

https://doi.org/10.1371/journal.pone.0191780.t004

from carbonate minerals with higher Sr concentration and a lower ^{87}Sr/^{86}Sr ratio, and the other part is provided by relatively stable silicate minerals with lower Sr concentration and a higher ^{87}Sr/^{86}Sr ratio. In a hot and humid environment, Ca and Sr in carbonate minerals are easily leached and migrated, resulting in an increase of the ^{87}Sr/^{86}Sr ratios in the residual soil [62, 66]. Profile PG is a typical terra rossa profile which presents slight alkaline environment (pH values of profile PG range from 6.89–7.79 (Table 2)) and relatively high CaO content and therefore, the significant negative correlation ($R^2 = 0.96$) between the CaO contents and ^{87}Sr/^{86}Sr ratios reflects the weathering and leaching processes of carbonate minerals (Fig 6C). On the contrary, profile XY is an acid lateritic weathering crust (pH values of profile XY range from 4.24–4.64 (Table 1)) which presents a complete decalcification hence CaO contents and ^{87}Sr/^{86}Sr ratios do not present any significant linear relations. However, compared with the mottled clay layer, the Fe nodular horizon has higher CaO contents and lower ^{87}Sr/^{86}Sr ratios, implying the lower ^{87}Sr/^{86}Sr ratios are possibly associated with Ca-bearing minerals. To a large extent, the Ca-bearing mineral is not carbonate, because of the strong eluviation and acid environment. The following discussion suggests the Ca-bearing mineral might possibly be apatite.

The Fe_2O_3 contents and ^{87}Sr/^{86}Sr ratios in profile XY have significant negative correlations, especially in the Fe nodular horizon ($R^2 = 0.90$) (Fig 6D). It indicates that the Fe_2O_3 contents have certain effects on controlling the Sr isotopic composition, particularly for the Fe nodular horizon. Although it has been proven that iron oxides/hydroxides have strong adsorption ability for Sr [67], the influence of the adsorption and coprecipitation of Fe oxides/hydroxides on Sr isotopic fractionation appears less than likely because Sr isotopes are infrequently fractionated by near-surface chemical, physical, and biological processes [31]. Based on studies of Fe nodules in weathered crust formed by granodioritic gneisses in the Mysore Plateau of southern India, Tripathi and Rajamani [36] proposed that discrete amorphous Mn phases (e.g., todorokite [(Ca,

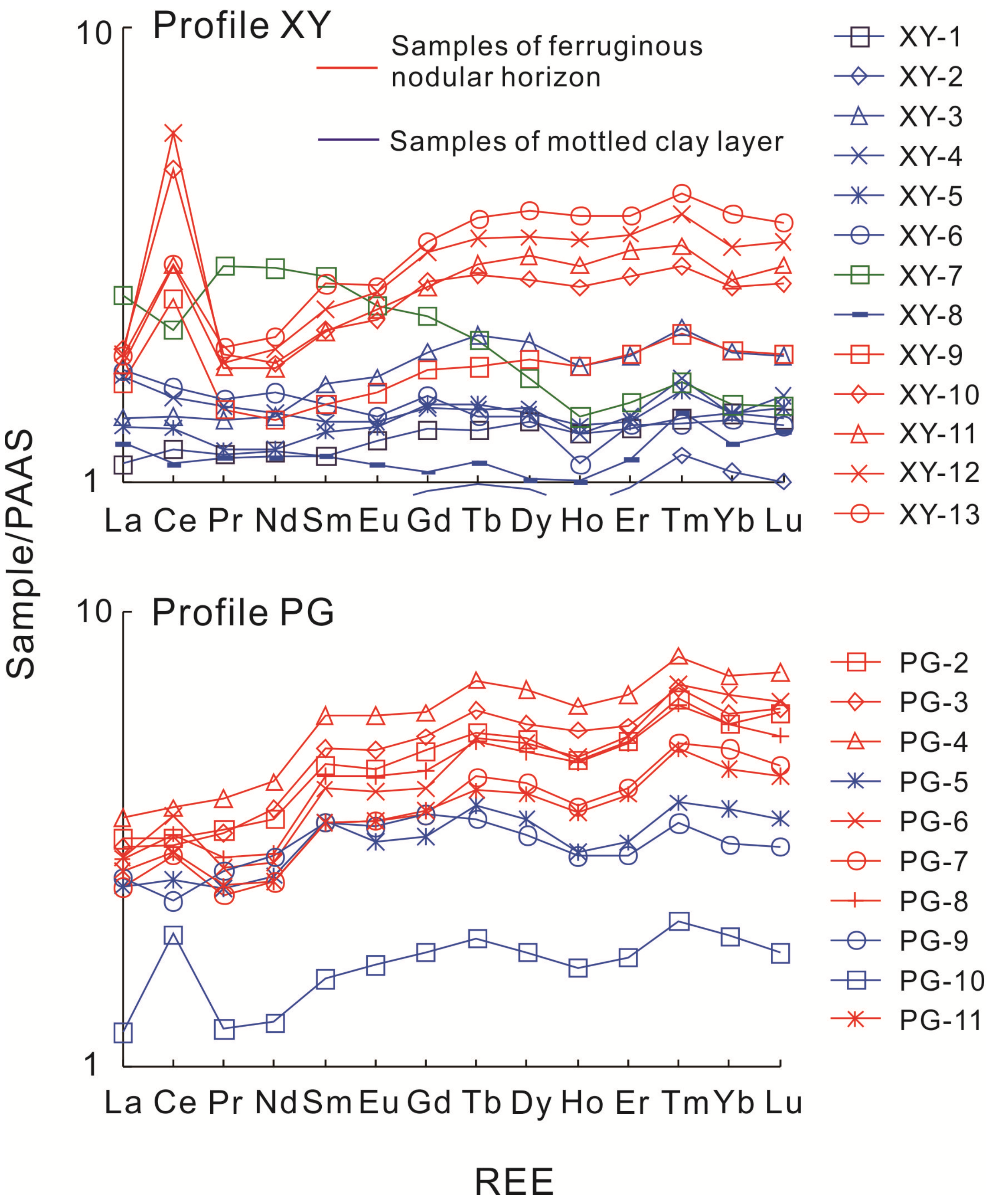

Fig 5. PAAS (Post–Archean Australian Shale) normalized REE distribution patterns of profiles XY and PG.

https://doi.org/10.1371/journal.pone.0191780.g005

Na, K) $_{0.3-0.5}$ Mn (IV or III), Mg] $_6$ O$_{12}$ (3–4.5) H_2O) concentrate trace elements including Sr. Todorokite is a mineral bearing K, Rb, and Sr and therefore, the content of todorokite in Fe nodules possibly influences the variation of the Sr isotope; however, discrete amorphous Mn phases were not observed in this study.

The result shows that weathering and decomposition of illite is one possible controlling factor of the Sr isotopic composition in the Fe nodular horizon. This is because the K_2O

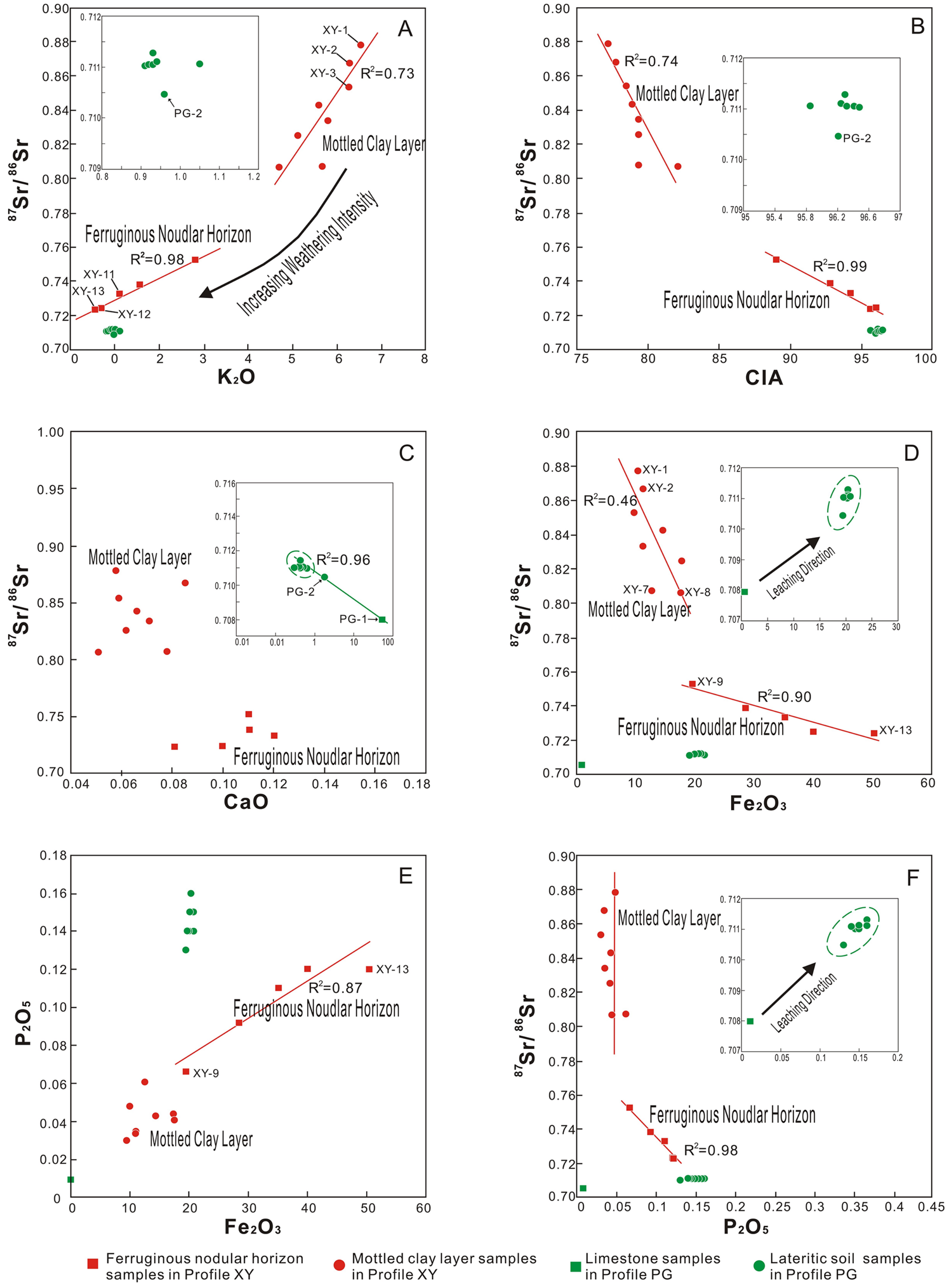
A
XY-1
XY-2
XY-3
R^2=0.73
Mottled Clay Layer
PG-2
Increasing Weathering Intensity
Ferruginous Noudlar Horizon
R^2=0.98
XY-11
XY-13
XY-12
$^{87}Sr/^{86}Sr$
K_2O
B
R^2=0.74
Mottled Clay Layer
PG-2
R^2=0.99
Ferruginous Noudlar Horizon
CIA
C
Mottled Clay Layer
R^2=0.96
PG-2
PG-1
Ferruginous Noudlar Horizon
CaO
D
XY-1
XY-2
R^2=0.46
XY-7
XY-8
Mottled Clay Layer
Leaching Direction
XY-9
R^2=0.90
Ferruginous Noudlar Horizon
XY-13
Fe_2O_3
E
XY-13
R^2=0.87
Ferruginous Noudlar Horizon
XY-9
Mottled Clay Layer
P_2O_5
F
Mottled Clay Layer
Leaching Direction
Ferruginous Noudlar Horizon
R^2=0.98
🟥 Ferruginous nodular horizon samples in Profile XY
● Mottled clay layer samples in Profile XY
🟩 Limestone samples in Profile PG
● Lateritic soil samples in Profile PG

Fig 6. Distributions of $^{87}Sr/^{86}Sr$ ratio with (A) K_2O, (B) CIA value, (C) CaO, (D) Fe_2O_3, and (F) P_2O_5 and relationships between (E) Fe_2O_3 and P_2O_5. Significant correlations are shown in the plots. CaO refers to the total content.

https://doi.org/10.1371/journal.pone.0191780.g006

concentration decreases with the increase of weathering intensity, and a significant positive correlation between K_2O and the $^{87}Sr/^{86}Sr$ ratio is present in the Fe nodular horizon ($R^2 = 0.98$) (Fig 6A). However, the positive correlation in the Fe nodular horizon appears to differ from that in the mottled clay layer (slopes of the two trend lines are different) (Fig 6A), which implies there is another factor controlling the Sr isotopic composition in the Fe nodular horizon or the mottled clay layer.

A relative accumulation of P_2O_5 and a significant linear relationship between P_2O_5 and Fe_2O_3 are found in the Fe nodular horizon (Fig 6E). This indicates that the Fe nodular horizon has strong adsorption and fixation to phosphate minerals [68–72]. According to the PAAS normalized REE pattern (Fig 5), compared with the mottled clay, the Fe nodules are characterized by high ΣREE and Sm_N/Nd_N ratio (N represents PAAS normalized), MREE and HREE enrichment, and depleted LREE (except Ce). The concentrations of P_2O_5, Sr, Th, and U are higher in the Fe nodular horizon than in the mottled clay layer. Generally, MREE-enriched apatite contains abundant REEs, Th, U, and Sr and the weathering of apatite might cause strong REE fractionation [44, 73–81]. Consequently, apatite can be interpreted as the main phosphate phase in Fe nodules, although phosphate minerals were not detected by the XRD analysis. This is probably because phosphate mineral abundances are low in the study profiles [82] but their existence is verified by geochemical data (Tables 1 and 2).

Apatite is an important common mineral in various rocks (including igneous, metamorphic, and sedimentary rocks), sediments, and alluvial and residual deposits. Primary apatite is generally considered a type of Rb-free mineral with no radiogenic ^{87}Sr [80], whereas secondary apatite might borrow radiogenic ^{87}Sr from the ambient diagenetic fluid [80, 83], which means apatite generally has a lower $^{87}Sr/^{86}Sr$ ratio. A significant negative correlation between the P_2O_5 contents and $^{87}Sr/^{86}Sr$ ratios ($R^2 = 0.98$) is observed in the Fe nodular horizon in profile XY (Fig 6F), which suggests that apatite fixed by Fe oxides is another mineralogical controlling factor of the Sr isotopic composition in the Fe nodular horizon.

Significance of Sr isotopes for evaluating weathering components and processes

In a typical geochemical weathering process for igneous rocks, Sr isotope variation is commonly associated with the leaching loss of Sr. Niobium (Nb) is an immobile element and hence, the concentration of Nb in soil solution is very low and the Nb/Sr ratio approaches zero. The concentration of Nb and the Nb/Sr ratio in soils is expected to increase as the degree of weathering increases. For this reason, $^{87}Sr/^{86}Sr$ versus Nb/Sr diagrams are generally used to evaluate the active Sr endmembers and to reveal the evolutionary processes of weathering profiles [32, 66, 84].

In profile XY, compared with the Fe nodular horizon, the mottled clay layer shows higher $^{87}Sr/^{86}Sr$ and lower Nb/Sr ratios (Fig 7). This illustrates the absolute Sr concentration decreases with increasing weathering intensity. The change of the $^{87}Sr/^{86}Sr$ ratio is associated mainly with the weathering and decomposition of illite; hence, the $^{87}Sr/^{86}Sr$ and Nb/Sr ratios do not show significant correlations in the mottled clay layer. However, the significant negative correlation ($R^2 = 0.99$) in the Fe nodular horizon is a geochemical response of the proportions of Fe nodules and clay. In the Fe nodular horizon, increasing weathering intensity causes the content of Fe nodules to increase, whereas the clay content decreases (Fig 2). The decreased clay content results in decreased Sr concentrations and low Nb/Sr ratios. Meanwhile, the increase

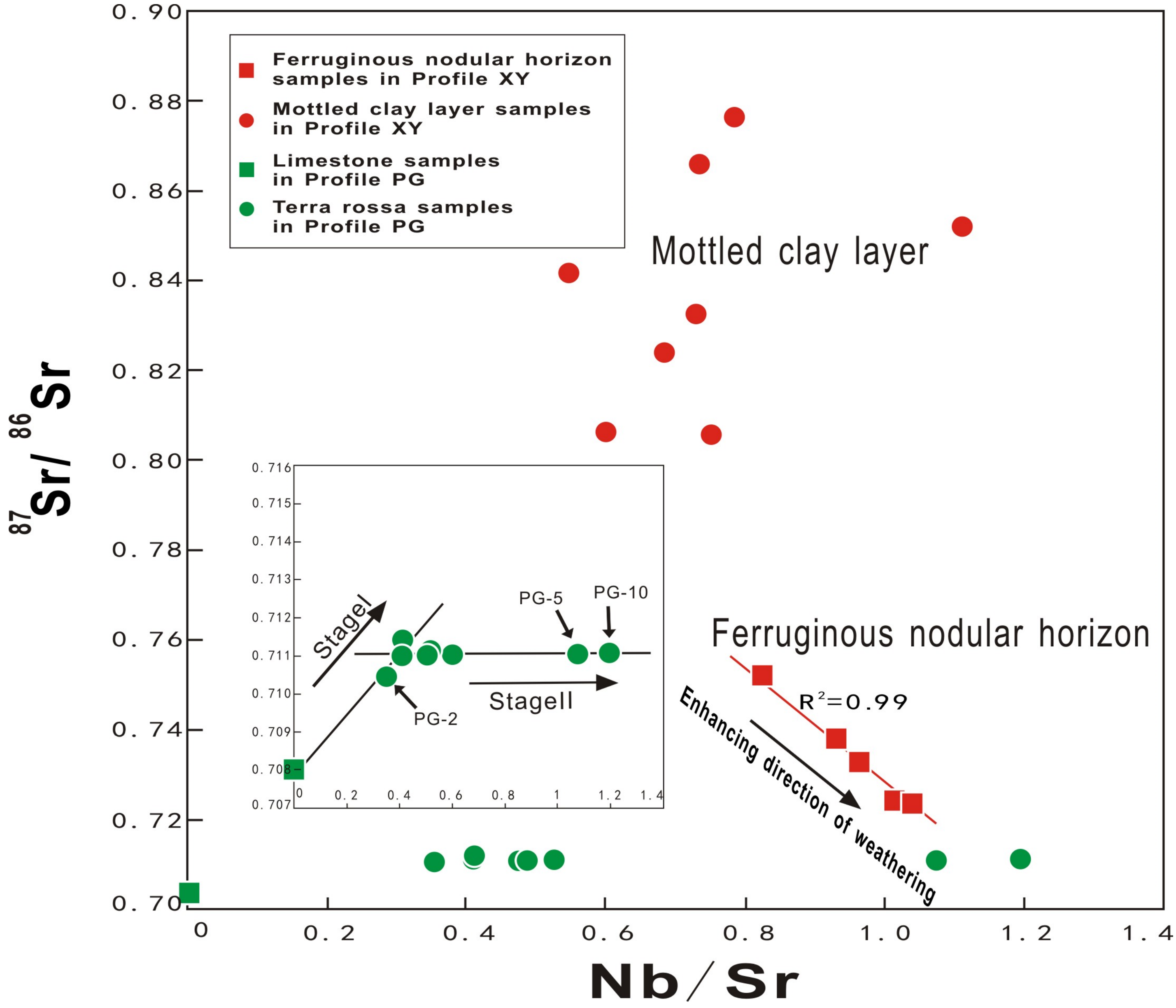

Fig 7. $^{87}Sr/^{86}Sr$ **ratio trends as function of Nb/Sr ratio in profiles XY and PG.**

https://doi.org/10.1371/journal.pone.0191780.g007

of Fe nodules benefits the fixation of apatite, which results in the decreased $^{87}Sr/^{86}Sr$ ratios in the Fe nodular horizon.

In Fig 7, the weathering front sample (PG–2) of profile PG is located between samples of bedrock and lateritic soil, implying binary mixing of two different Sr isotopic endmembers. A leaching experiment confirmed two distinct Sr isotopic sources in the carbonate rock: the carbonate and silicate mineral endmembers [62]. The carbonate endmember largely represents the Sr isotopic signature of seawater in the diagenesis period, whereas the silicate endmember is a label of the Sr isotopic composition of fragments from the weathering of continental rock. Because of the observably different rates of weathering between carbonate and silicate minerals, the weathering process of carbonate rocks can be divided into two stages [8]: Stage I representing the leaching process of carbonate minerals and stage II representing the weathering process of saprolite (Fig 7).

Fresh bedrock commonly represents the carbonate endmember with a relatively lower $^{87}Sr/^{86}Sr$ ratio and higher Sr content, because carbonate minerals take a dominant position over silicate impurities in the contents of carbonate rocks. Carbonate minerals are weathered preferentially under warm and humid conditions and thus, the silicate endmember with a higher $^{87}Sr/^{86}Sr$ ratio controls the Sr isotopic composition in saprolite. Therefore, Stage I presents a trend of increase in the $^{87}Sr/^{86}Sr$ ratio and a reduction in Sr content (Fig 7). In stage II, carbonates are exhausted (CaO concentration usually <0.5 wt.%) and silicate components constitute the main body of the regolith. During this process, silicate minerals suffer the effects of long periods of strong weathering and they transform into more stable minerals, such as kaolinite and gibbsite. Samples in the regolith of profile PG are distributed along a line that nearly parallels the Nb/Sr axis (Fig 7). However, samples PG–5 and PG–10 show higher Nb/Sr ratios, which might possibly be due to lower apatite contents (Figs 4 and 5). Results indicate that the changes in Sr concentration do not yield obvious alteration in the $^{87}Sr/^{86}Sr$ ratios. The constant $^{87}Sr/^{86}Sr$ ratios suggest that several main Sr-bearing carbonate minerals have been completely weathered and the residual Sr in the regolith might possibly have a similar $^{87}Sr/^{86}Sr$ ratio.

Implications of Sr isotopes for material source tracing and paleogeographic reconstruction

In radioactive isotope chronology, the Rb–Sr isotope pair is commonly used to evaluate the crystallization age and sedimentary age of a closed rocky system [59, 85]. In the open supergene environment, however, weathering usually results in variations of the Rb and Sr concentrations and leaching rates of radiogenic and non-radiogenic Sr because of the diverse weathering rates of different minerals [43, 45–46, 61, 86–87]. Generally, minerals with high Rb/Sr ratios have high $^{87}Sr/^{86}Sr$ ratios and good resistance to weathering. If the radiogenic ^{87}Sr in the weathering cover were primarily from the beta decay of ^{87}Rb, then the weathering and decomposition of Rb-bearing minerals would lead to the loss of Rb and radiogenic ^{87}Sr from the weathering system. The Rb/Sr and $^{87}Sr/^{86}Sr$ ratios of the two weathering profiles in the studied area show significant positive correlation ($R^2 = 0.97$ in profile XY and $R^2 = 0.78$ in profile PG) (Fig 8A). The strong linear relationships of the two weathering covers indicate radiogenic ^{87}Sr is derived mainly from ^{87}Rb decay, and the contribution from allothogenic ^{87}Sr is very limited. In comparison with profile PG, the Rb/Sr and $^{87}Sr/^{86}Sr$ ratios of profile XY, especially in the mottled clay layer, are higher and spread over a larger interval, presumably because of the lesser degree of weathering and because the parent rock contained abundant minerals with high Rb/Sr ratios [88].

In geological history, the $^{87}Sr/^{86}Sr$ ratio of seawater was in dynamic equilibrium and therefore, the $^{87}Sr/^{86}Sr$ ratios of carbonate rocks deposited at that time should reflect the Sr isotope compositional signature of the seawater [43, 89–91]. Similarly, lateritic soils weathered from carbonate rocks could contain real geological information concerning the terrigenous detrital material of the source region [92].

To explore the Sr isotope source of weathering covers, the study profiles are compared with some analogous lateritic weathering profiles in Guizhou Province (Fig 8B). Some of the data are from published reports [62, 93] and the basic information of the weathering profiles is listed in the table in Fig 8B. In Fig 8B, lateritic soil samples are divided into two distinct groups according to the ages of the bedrock: Group T (bedrock is from the Triassic) and Group P (bedrock is from the Permian). In Group P, samples of profiles PG, QZ-III and BY are located

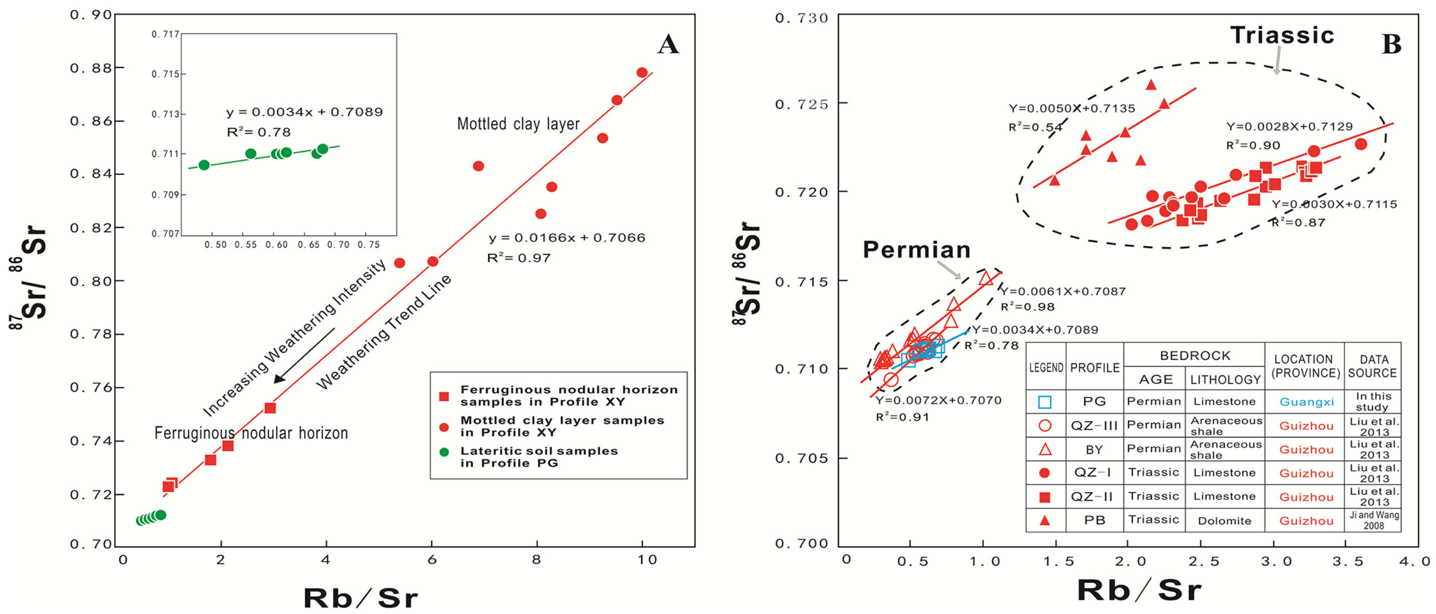

LEGEND	PROFILE	BEDROCK		LOCATION (PROVINCE)	DATA SOURCE
		AGE	LITHOLOGY		
□	PG	Permian	Limestone	Guangxi	In this study
○	QZ–III	Permian	Arenaceous shale	Guizhou	Liu et al. 2013
△	BY	Permian	Arenaceous shale	Guizhou	Liu et al. 2013
●	QZ–I	Triassic	Limestone	Guizhou	Liu et al. 2013
■	QZ–II	Triassic	Limestone	Guizhou	Liu et al. 2013
▲	PB	Triassic	Dolomite	Guizhou	Ji and Wang 2008

Fig 8. Relationships between ^{87}Sr/^{86}Sr and Rb/Sr ratios. (A) Weathering profiles in the studied area. (B) cited profiles in Guizhou province. (Data of profiles PB were derived from Ji and Wang [93]; data of profiles QZ–I, QZ–II, QZ–III and BY are from Liu et al. [62]).

https://doi.org/10.1371/journal.pone.0191780.g008

in an adjacent area and they have similar intercepts for their regression equations (0.7070, 0.7087, and 0.7089, respectively). It indicates that, in the Permian, the area that contained Guangxi and Guizhou provinces (and possibly even a wider geographical area) was a big sedimentary basin with the same source of continental material. The situation is similar for Group T with the samples also having similar intercepts (0.7115, 0.7129, and 0.7135). However, Group T has higher Rb/Sr and ^{87}Sr/^{86}Sr ratios than Group P, implying that the continental fragment source of the South China sedimentary basin must have changed dramatically from the Permian to the Triassic. These changes of continental material source were possibly associated with plate tectonic activities. According to the lithofacies paleogeography, global plate arrangements during the Late Paleozoic were dominated by the supercontinent Pangea, bounded to the west by the Panthalassa Ocean and to the east by the tropical Tethys seaway (Fig 9). During the Late Permian, China consisted of several isolated small continents that existed in the Tethys seaway. During the late Triassic, the North China and South China blocks collided and migrated northward, until eventually colliding with Siberia (Fig 9) [94–95]. Therefore, the Sr isotopic records in lateritic soils likely provide evidence for the movement of the South China block during the Late Paleozoic.

Compared with profiles QZ–III and BY, profile PG presents a slightly lower ^{87}Sr/^{86}Sr ratio and a smaller slope of its regression equation (PG: 0.0034, BY: 0.0061, and QZ: 0.0072) (Fig 8B). The lower ^{87}Sr/^{86}Sr ratio suggests that the source area provided more radiogenic ^{87}Sr terrigenous detrital material to the Guizhou area than to Guangxi. The smaller slope of the regression equation indicates that profile PG has experienced a higher degree of weathering than the other two profiles (QZ–III and BY). Generally, fine grain size fractions in weathering products represent highly weathered mineral facies, whereas coarse grain size fractions indicate weak weathering. Aubert et al. [44] proposed that the coarse grain size fractions of soils are more radiogenic than the fine grain size fractions. According to the principles of water transportation and deposition, coarse grain size materials are deposited preferentially. Thus, from the Sr isotopic composition of weathering covers in Guizhou and Guangxi provinces, we can infer

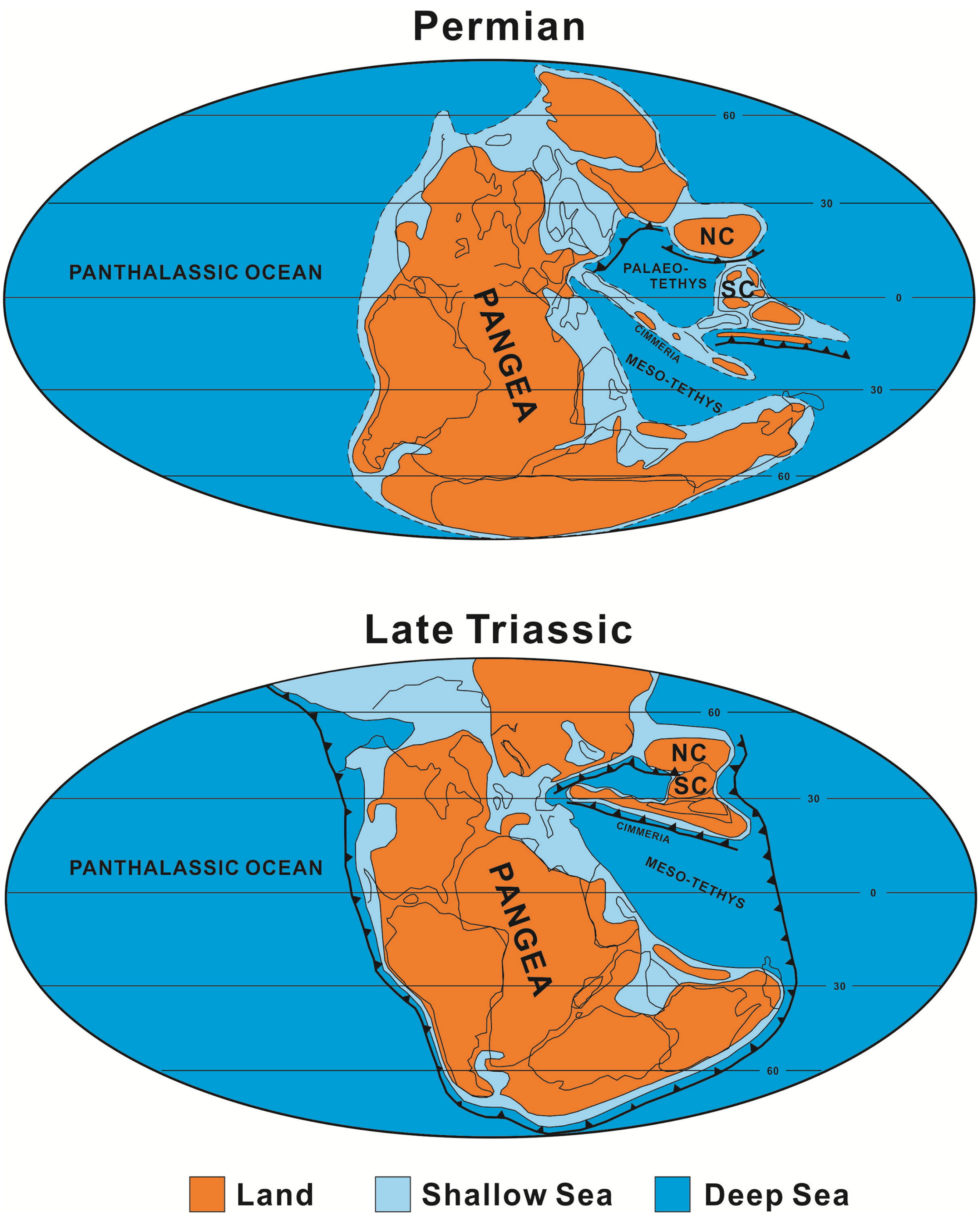
Permian
PANTHALASSIC OCEAN
PANGEA
NC
SC
PALAEO-TETHYS
CIMMERIA
MESO-TETHYS
60
30
0
30
60
Late Triassic
PANTHALASSIC OCEAN
PANGEA
NC
SC
CIMMERIA
MESO-TETHYS
60
30
0
30
60
Land
Shallow Sea
Deep Sea

Fig 9. Global paleogeographic reconstruction in the Permian and the Late Triassic. NC: North China, SC: South China (after Scotese and Ziegler [96]).

https://doi.org/10.1371/journal.pone.0191780.g009

that in the diagenetic period of the carbonate rocks (approximately from the Permian to the Middle Triassic), the Guizhou area was closer than the Guangxi area to the continental source. Relatively, the Guangxi region was further from the continental source and thus, it accepted epicontinental sea or hemipelagic deposition. The lithofacies paleogeography suggests that, in the Late Paleozoic, transgressions in the studied area always spread from south to north. The northern part of the Guizhou area was located in the Yangtze craton, whereas the Guangxi remained situated in the ancient sedimentary basin [97–99].

Conclusions

An investigation was performed that used mineralogy, element geochemistry, and Sr isotope ratios to assess the Sr isotope geochemical characteristics and weathering processes of carbonate rock regolith. The results indicated that the mineral compositions and abundances in lateritic soils have an obvious effect on the Sr isotopic compositional signature. For example, weathering and decomposition of illite was found to be the primary factor that caused significant change of the Sr isotopic composition in profile XY that is an argillaceous limestone weathering crust with a lower weathering intensity. In addition, the major and trace element distributions in the vertical direction, REE distribution patterns, and Sr isotopic compositions showed that the accumulation of apatite, together with the adsorption and precipitation of Fe oxides/hydroxides, might possibly be another controlling factor of the Sr isotopic composition in the Fe nodular horizon. However, the weathering and dissolution of carbonate minerals (e.g., calcite and dolomite) in profile PG that is a limestone weathering crust with a higher weathering intensity were found to result in an increase of the $^{87}Sr/^{86}Sr$ ratio in the residual weathering products compared with the parent rock.

During the weathering and pedogenesis process of carbonate rocks, the leaching of carbonate minerals resulted in the increased $^{87}Sr/^{86}Sr$ ratio in the residual soils. When the carbonate components were leached out, the compositions and concentrations of silicate phases would largely dominated the $^{87}Sr/^{86}Sr$ ratio signatures. In addition, the proportional quantities of Fe nodules and clay are critical for controlling the Sr isotopic signature of the Fe nodular horizon in the typical lateritic weathering covers in Guangxi Province.

The results of this study suggest that parent rocks provided the main Sr isotopic source to the overlying weathering covers within the studied area, and that the contributions from allothogenic Sr isotopes were limited. The continental fragment source of the South China sedimentary basin changed dramatically from the Permian to the Triassic. This provides geochemical support for the movement of the South China block during the Late Paleozoic. In the Permian, the areas of Guizhou and Guangxi were located within the same sedimentary basin; however, the Guizhou area was closer to the continental source area, whereas the Guangxi region possibly accepted epicontinental sea or hemipelagic deposition.

Acknowledgments

We appreciate Prof. Chongshan Liang, Guohong Gong and Mu Liu for the help in TIMS, XRD and ICP–MS test and analytical works, respectively. We are indebted to Prof. Congqiang Liu for comments and suggestion about this manuscript.

Author Contributions

Conceptualization: Hongbing Ji.

Data curation: Hongbing Ji.

Formal analysis: Xiao Wei, Shijie Wang, Hongbing Ji, Zhenhua Shi.

Funding acquisition: Shijie Wang, Hongbing Ji.

Investigation: Xiao Wei, Hongbing Ji.

Methodology: Xiao Wei, Hongbing Ji.

Project administration: Shijie Wang, Hongbing Ji.

Resources: Shijie Wang, Hongbing Ji.

Supervision: Shijie Wang, Hongbing Ji.

Writing – original draft: Xiao Wei.

Writing – review & editing: Shijie Wang, Hongbing Ji, Zhenhua Shi.

References

1. Bouchard M., Jolicoeur S. Chemical weathering studies in relation to geomorphological research in southeastern canada. Geomorphology. 2000; 32(3):213–238.
2. Chesworth W, Dejou J, Larroque P. The weathering of basalt and relative mobilities of the major elements at Belbex, France. Geochimica et Cosmochimica Acta. 1981; 45:1235–1243.
3. Harley AD, Gilkes RJ. Factors influencing the release of plant nutrient elements from silicate rock powders: a geochemical overview. Nutrient Cycling in Agroecosystems. 2000; 56(1):11–36.
4. Meybeck M. Global chemical weathering of surficial rocks estimated from river dissolved loads. American Journal of Science. 1987; 287(5):401–428.
5. Braun JJ, Pagel M, Muller JP, Bilong P, Michard A, Guillet B. Cerium anomalies in lateritic profiles. Geochimica et Cosmochimica Acta. 1990; 54(3):781–795.
6. Nesbitt HW, Wilson RE. Recent chemical weathering of basalt. American Journal of Science. 1992; 292 (10):740–777.
7. White AF, Blum AE. Effects of climate on chemical_weathering in watersheds. Geochimica et Cosmochimica Acta. 1995; 59(9):1729–1747.
8. Wang S, Ji H, Ouyang Z, Zhou D, Zheng L, Li T. Preliminary study on weathering and pedogenesis of carbonate rock. Sci. China, Ser. D. 1999; 42:572–581. Chinese.
9. Dessert C, Dupré B, Gaillardet J, François LM, Allegre CJ. Basalt weathering laws and the impact of basalt weathering on the global carbon cycle. Chemical Geology. 2003; 202(3):257–273.
10. Muhs DR, Ager TA, Skipp G, Beann J, Budahn J, McGeehin JP. Paleoclimatic significance of chemical weathering in loess–derived paleosols of subarctic central Alaska. Arctic, Antarctic, and Alpine Research. 2008; 40(2):396–411.
11. Dixon JL, Hartshorn AS, Heimsath AM, DiBiase RA, Whipple KX. Chemical weathering response to tectonic forcing: A soils perspective from the San Gabriel Mountains, California. Earth and Planetary Science Letters. 2012; 323:40–49.
12. Blum JD, Erel Y, Brown K. ^{87}Sr/^{86}Sr ratios of sierra nevada stream waters: Implications for relative mineral weathering rates. Geochimica et Cosmochimica Acta. 1993; 57(21): 5019–5025.
13. Bain DC, Bacon JR. Strontium isotopes as indicators of mineral weathering in catchments. Catena. 1994; 22(3):201–214.
14. Douglas GB, Gray CM, Hart BT, Beckett R. A strontium isotopic investigation of the origin of suspended particulate matter (SPM) in the Murray–Darling River system, Australia. Geochimica et Cosmochimica Acta. 1995; 59(18):3799–3815.
15. Land M, Ingri J, Andersson PS, Öhlander B. Ba/Sr, Ca/Sr and ^{87}Sr/^{86}Sr ratios in soil water and groundwater: implications for relative contributions to stream water discharge. Applied Geochemistry. 2000; 15 (3):311–325.
16. Chung CH, You CF, Chu HY. Weathering sources in the Gaoping (Kaoping) river catchments, southwestern Taiwan: Insights from major elements, Sr isotopes, and rare earth elements. Journal of Marine Systems. 2009; 76(4):433–443.

17. Pett–Ridge JC, Derry LA, Kurtz AC. Sr isotopes as a tracer of weathering processes and dust inputs in a tropical granitoid watershed, Luquillo Mountains, Puerto Rico. Geochimica et Cosmochimica Acta,. 2009; 73(1):25–43.
18. Wei G, Ma J, Liu Y, Xie L, Lu W, Deng W, Yang Y. Seasonal changes in the radiogenic and stable strontium isotopic composition of Xijiang River water: Implications for chemical weathering. Chemical Geology. 2013; 343:67–75.
19. Musgrove M, Banner JL. Regional ground–water mixing and the origin of saline fluids: Midcontinent, United States. Science. 1993; 259(5103):1877–1882. https://doi.org/10.1126/science.259.5103.1877 PMID: 17836245
20. Johnson TM, DePaolo DJ. Interpretation of isotopic data in groundwater–rock systems: model development and application to Sr isotopic data from Yucca Mountain. Water Resources Research. 1994; 30:1571–1587.
21. Bullen TD, Krabbenhoft DP, Kendall C. Kinetic and mineralogic controls on the evolution of groundwater chemistry and $^{87}Sr/^{86}Sr$ in a sandy silicate aquifer, northern Wisconsin. Geochimica et Cosmochimica Acta. 1996; 60:1807–1821.
22. Klaus JS, Hansen BT, Buapeng S. $^{87}Sr/^{86}Sr$ ratio: a natural tracer to monitor groundwater flow paths during artificial recharge in the Bangkok area, Thailand. Hydrogeology Journal. 2007; 15:745–758.
23. Cartwright I, Weaver T, Petrides B. Controls on $^{87}Sr/^{86}Sr$ ratios of groundwater in silicate–dominated aquifers: SE Murray Basin, Australia. Chemical Geology, 2007; 246:107–123.
24. Raiber M, Webb JA, Bennetts DA. Strontium isotopes as tracers to delineate aquifer interactions and the influence of rainfall in the basalt plains of southeastern Australia. Journal of hydrology. 2009; 367 (3):188–199.
25. Krabbenhöft A, Eisenhauer A, Böhm F, Vollstaedt H, Fietzke J, Liebetrau V, et al. Constraining the marine strontium budget with natural strontium isotope fractionations ($^{87}Sr/^{86}Sr^*$, $\delta^{88}/^{86}Sr$) of carbonates, hydrothermal solutions and river waters. Geochimica et Cosmochimica Acta. 2010; 74(14):4097–4109.
26. Borg LE, Banner JL. Neodymium and strontium isotopic constraints on soil sources in Barbados, West Indies. Geochimica et Cosmochimica Acta. 1996; 60(21):4193–4206.
27. Drouet T, Herbauts J, Gruber W, Demaiffe D. Strontium isotope composition as a tracer of calcium sources in two forest ecosystems in Belgium. Geoderma. 2005; 126(3):203–223.
28. Hartman G, Richards M. Mapping and defining sources of variability in bioavailable strontium isotope ratios in the Eastern Mediterranean. Geochimica et Cosmochimica Acta. 2014; 126:250–264.
29. Edmond JM. Himalayan tectonics, weathering processes, and the strontium isotope record in marine limestones. Science. 1992; 258(5088):1594–1597. https://doi.org/10.1126/science.258.5088.1594 PMID: 17742524
30. Raymo ME, Ruddiman WF. Tectonic forcing of late Cenozoic climate. Narure. 1992; 359:117–122.
31. Graustein WC. $^{87}Sr/^{86}Sr$ ratios measure the sources and flow of strontium in terrestrial ecosystems. In Stable isotopes in ecological research. Springer New York. 1989;491–512.
32. Bullen T, White A, Blum A, Harden J, Schulz M. Chemical weathering of a soil chronosequence on granitoid alluvium: II. Mineralogic and isotopic constraints on the behavior of strontium. Geochimica et Cosmochimica Acta. 1997; 61(2):291–306.
33. Åberg G, Jacks G, Joseph Hamilton P. Weathering rates and $^{87}Sr/^{86}Sr$ ratios: An isotopic approach. Journal of Hydrology. 1989; 109(1):65–78.
34. Brass GW. The effect of weathering on the distribution of strontium isotopes in weathering profiles. Geochimica et Cosmochimica Acta. 1975; 39(12):1647–1653.
35. Crerar DA, Barnes HL. Deposition of deep–sea manganese nodules. Geochimica et Cosmochimica Acta. 1974; 38(2):279–300.
36. Tripathi JK, Rajamani V. Geochemistry and origin of ferruginous nodules in weathered granodioritic gneisses, mysore plateau, southern India. Geochimica et Cosmochimica Acta. 2007; 71(7):1674–1688.
37. Löhr SC, Grigorescu M, Cox ME. Iron nodules in ferric soils of the Fraser Coast, Australia: relicts of laterisation or features of contemporary weathering and pedogenesis? Soil Research. 2013; 51(2):77–93.
38. Burns RG, Burns VM. Mechanism for nucleation and growth of manganese nodules. Nature. 1975; (5504):130–131.
39. Palumbo B, Bellanca A, Neri R, Roe MJ. Trace metal partitioning in Fe-Mn nodules from sicilian soils, Italy. Chemical Geology. 2001; 173(4):257–269.
40. Schulz MS, Vivit D, Schulz C, Fitzpatrick J, White A. Biologic origin of iron nodules in a marine terrace chronosequence, Santa Cruz, California. Soil Science Society of America Journal. 2010; 74:550–564.

41. González FJ, Somoza L, León R, Medialdea T, Torres T, Ortiz JE, et al. Ferromanganese nodules and micro-hardgrounds associated with the Cadiz Contourite Channel (NE Atlantic): Palaeoenvironmental records of fluid venting and bottom currents. Chemical Geology. 2012; 310–311:56–78

42. Dubinin AV, Uspenskaya TY, Rimskaya-Korsakova MN, Demidova TP. Rare Elements and Nd and Sr Isotopic Composition in Micronodules from the Brazil Basin, Atlantic Ocean. Lithology and Mineral Resources. 2017; 52:81–101.

43. Blum JD, Erel Y. A silicate weathering mechanism linking increases in marine $^{87}Sr/^{86}Sr$ with global glaciation. Nature. 1995; 373 (6513):415–418.

44. Aubert D, Stille P, Probst A. REE fractionation during granite weathering and removal by waters and suspended loads: Sr and Nd isotopic evidence. Geochimica et Cosmochimica Acta. 2001; 65(3):387–406.

45. Ma Y, Liu C. Evolution of Sr isotope during the Chemical weathering process of granite: Influence of mineral relative weathering rate. Science in China (Series: D). 2001; 31(8):634–640. Chinese.

46. Erel Y, Blum JD, Roueff E, Ganor J. Lead and strontium isotopes as monitors of experimental granitoid mineral dissolution. Geochimica et Cosmochimica Acta. 2004; 68(22):4649–4663.

47. Hissler C, Stille P, Juilleret J, Iffly JF, Perrone T, Morvan G. Elucidating the formation of terra fuscas using Sr–Nd–Pb isotopes and rare earth elements. Applied Geochemistry. 2015; 54:85–99.

48. Braun JJ, Marechal JC, Riotte J, Boeglin JL, Bedimo Bedimo JP, Ndam Ngoupayou JR, et al. Elemental weathering fluxes and saprolite production rate in a Central African lateritic terrain (Nsimi, South Cameroon). Geochimica et Cosmochimica Acta. 2012; 99:243–270.

49. Zhou F, Mei X. Geological characteristics of Guigang–type bauxite deposit. Light Mental. 1992; 11:1–7. Chinese.

50. Wei X, Ji H, Wang S, Chu H, Song C. The formation of representative lateritic weathering covers in south–central Guangxi (southern China). Catena. 2014; 118:55–72.

51. Wang S, Ji H, Sun C. Preliminary study on REE distribution characteristics in dolomite weathering profile in Pingba County, Guizhou. Chinese Journal of Geology. 2001; 36 (4): 474–480. Chinese.

52. Nesbitt HW, Young GM. Early Proterozoic climates and plate motions inferred from major element chemistry of lutites. Nature. 1982; 299(5885):715–717.

53. Mclennan SM, Hemming S, Niel DK, Hanson GN. Geochemical approaches to sedimentation, provenance, and tectonics. Geological Society of America Special Papers. 1993; 284:21–40.

54. Fedo CM, Nesbitt HW, Young GM. Unraveling the effects of potassium metasomatism in sedimentary rocks and paleosols, with implications for paleoweathering conditions and provenance. Geology. 1995; 23(1995):921–924.

55. Blake GR, Hartge KH. Bulk density. Methods of Soil Analysis, Part 1: Physical and Mineralogical Methods; Klute A. (ed.); Soil Science Society of America: Madison, Wisconsin. 1986; 363–375.

56. Taylor SR, McLennan SM. Continental Crust. Its Composition and Evolution. Blackwell Scientific Publications, London. 1985 (312 pp.)

57. Goldich SS, Gast PW. Effects of weathering on the RbSr and KAr ages of biotite from the Morton Gneiss, Minnesota. Earth and Planetary Science Letters. 1966; 1(6):372–375.

58. Dasch EJ. Strontium isotopes in weathering profiles, deep–sea sediments, and sedimentary rocks. Geochimica et Cosmochimica Acta. 1969; 33(12):1521–1552.

59. Faure G. Principles of isotope geology. New York: John Wiley & Son, Ltd.. 1977;177–199.

60. Faure G. The isotope geology of lead. Principles of isotope geology. 1986;309–340.

61. Blum JD, Erel Y. Rb–Sr isotope systematics of a granitic soil chronosequence: the importance of biotite weathering. Geochimica et Cosmochimica Acta. 1997; 61 (15):3193–3204.

62. Liu W, Liu C, Zhao Z, Xu Z, Liang C, Li L, et al. Elemental and strontium isotopic geochemistry of the soil profiles developed on limestone and sandstone in karstic terrain on Yunnan–Guizhou Plateau, China: Implications for chemical weathering and parent materials. Journal of Asian Earth Sciences. 2013; 67:138–152.

63. Gilkes RJ, Suddhiprakarn A. Biotite alteration in deeply weathered granite; I, Morphological, mineralogical, and chemical properties. Clays and Clay Minerals. 1979; 27(5): 349–360.

64. White AF, Yee A. Aqueous oxidation–reduction kinetics associated with coupled electron–cation transfer from iron–containing silicates at 25˚C. Geochimica et Cosmochimica Acta. 1985; 49(5):1263–1275.

65. Acker JG, Bricker OP. The influence of pH on biotite dissolution and alteration kinetics at low temperature. Geochimica et Cosmochimica Acta. 1992; 56(8):3073–3092.

66. Ji H, Wang S, Ouyang Z, Zhang S. A new model for determining the weathering components in red weathering crust over dolomites. Acta Geoscientia Sinica. 2003; 24:38–43. Chinese.

67. Axe L, Bunker GB, Anderson PR, Tyson TA. An XAFS analysis of strontium at the hydrous ferric oxide surface. Journal of Colloid & Interface Science. 1998; 199(1):44–52.
68. Borggaard OK. The influence of iron oxides on phosphate adsorption by soil. Journal of Science. 1983; 34(2):333–341.
69. Madrid L, Arambarri PD. Adsorption of phosphate by two iron oxides in relation to their porosity. Journal of Science. 1985; 36(4):523–530.
70. Shang C, Huang PM, Stewart JWB. Kinetics of adsorption of organic and inorganic phosphates by short–range ordered iron precipitate. Soil Science. (Trends in Agric. Sci.). 1993; 1:137–144.
71. Tiessen HK, Abekoe MH, Salcedo I, Owusu–bennoah E. Reversibility of phosphorus sorption by ferruginous nodules. Plant and Soil. 1993; 153(1):113–124.
72. Liu C, Huang PM. Kinetics of phosphate adsorption on iron oxides formed under the influence of citrate. Canadian Journal of Soil Science. 2000; 80:445–454.
73. Nagasawa H. Rare earth concentrations in zircons and apatites and their host dacites and granites. Earth and Planetary Science Letters. 1970; 9:359–364.
74. Gromet LP, Silver LT. Rare earth element distributions among minerals in a granodiorite and their petrogenetic implications. Geochimica et Cosmochimica Acta. 1983; 47:925–939.
75. Ohr M, Halliday AN, Peacor DR. Mobility and fractionation of rare earth elements in argillaceous sediments: inplications for dating diagenesis and low–grade metamorphism. Geochimica et Cosmochimica Acta. 1994; 58:289–312.
76. Weber ET, Owen RM, Dickens GR, Rea DK. Causes and implications of the middle rare earth element depletion in the eolian component of the North Pacific sediment. Geochimica et Cosmochimica Acta. 1998; 62:1735–1744.
77. Kazin PE, Karpov AS, Jansen M, Nuss J, Tretyakov Y. Crystal Structure and Properties of Strontium Phosphate Apatite with Oxocuprate Ions in Hexagonal Channels. Zeitschrift für anorganische und allgemeine Chemie. 2003; 629(2):344–352.
78. Köhler SJ, Harouiya N, Chaïrat C, Oelkers EH. Experimental studies of REE fractionation during water–mineral interactions: REE release rates during apatite dissolution from pH 2.8 to 9.2. Chemical Geology. 2005; 222:168–182.
79. Stille P, Stille MC, Pierret M, Steinmann F, Chabaux R, Boutin D, et al. Morvan Impact of atmospheric deposition, biogeochemical cycling and water–mineral interaction on REE fractionation in acidic surface soils and soil water (the Strengbach case). Chemical Geology. 2009; 264:173–186.
80. Castorina F, Masi U, DAntona M. REY and Sr–Nd isotopes of soils from Ravenna (Northern Italy) and their significance for environmental studies. Journal of Geochemical Exploration. 2014; 142:138–148.
81. Yang YH, Wu FY, Yang JH, Chew DM, Xie LW, Chu ZY. Sr and Nd isotopic compositions of apatite reference materials used in U–Th–Pb geochronology. Chemical Geology. 2014; 385: 35–55.
82. Cidu R, Antisari LV, Biddau R, Buscaroli A, Carbone S, Da Pelo S, et al. Dynamics of rare earth elements in water–soil systems: The case study of the Pineta San Vitale (Ravenna, Italy). Geoderma. 2013; 193–194(2):52–67.
83. Ovchinnikova GV, Kuznetsov AB, Vasil'eva IM, Gorokhov IM, Krupenin MT, Gorokhovskii BM, et al. Pb–Pb age and Sr isotopic characteristic of the Middle Riphean phosphorite concretions: The Zigaza–Komarovo Formation of the South Urals. Doklady Earth Sciences. 2013; 451(2):798–802.
84. White AF, Bullen TD, Schulz MS, Blum AE, Huntington TG, Peters NE. Differential rates of feldspar weathering in granitic regoliths. Geochimica et Cosmochimica Acta. 2001; 65(5): 847–869.
85. Chen J, Wang H. Geochemistry. Beijing: Science Press. 2004;145–148.
86. Clauer N. Strontium and argon isotopes in naturally weathered biotites, muscovites and feldspars. Chemical Geology. 1981; 31:325–334.
87. Brantley SL, Chesley JT, Stillings LL. Isotopic ratios and release rates of strontium measured from weathering feldspars. Geochimica et Cosmochimica Acta. 1998; 62(9):1493–1500.
88. Åberg G. The use of natural strontium isotopes as tracers in environmental studies. In Biogeochemical Monitoring in Small Catchments. Springer Netherlands. 1995; 79(79): 309–322.
89. Hodell DA, Mueller PA, McKenzie JA, Mead GA. Strontium isotope stratigraphy and geochemistry of the late Neogene ocean. Earth and Planetary Science Letters. 1989; 92(2):165–178.
90. Derry LA, France–Lanord C. Neogene Himalayan weathering history and river $^{87}Sr/^{86}Sr$: impact on the marine Sr record. Earth and Planetary Science Letters. 1996; 142(1):59–74.
91. Williamson T, Henderson RA, Price GD, Collerson KD. Strontium–isotope stratigraphy of the Lower Cretaceous of Australia. Cretaceous Research. 2012; 36:24–36.

92. Ji H, Ouyang Z, Wang S, Zhou D. Element geochemical characteristics of dolomite weathering profile and significance for average chemical composition of the upper continental crust. Science in China (Series D). 1999; 29(6):504–513. Chinese.

93. Ji H, Wang S. Sr-Nd isotope composition and evolution in a dolomite weathering profile in the central Guizhou province. Progress in Natural Science. 2008; 18(10):1128–1135. Chinese.

94. Lin JL, Fuller M, Zhang WY. Preliminary phanerozoic polar wander paths for the north and south china blocks. Nature. 1985; 313(6002):444–449.

95. Steiner M, Ogg J, Zhang Z, Sun S. The late permian/early triassic magnetic polarity time scale and plate motions of south china. Journal of Geophysical Research Solid Earth. 1989; 94(B6):7343–7363.

96. Scotese CR, Ziegler AM. Paleozoic base maps. Journal of Geology. 1979; 87(3):217–277.

97. Feng Z, He Y, Wu S. Listhofacies paleogeography of Permian Middle and Lower Yangtze region. Acta Sedimentologica Sinica. 1993; 11(3):13–24. Chinese.

98. Yin H, Tong J, Ding M, Zhang K, Lai X. Late Permian–Middle Triassic sea level changes of Yangtze Platform. Earth Science–Journal of China University of Geosciences. 1994; 19(5):627–632. Chinese.

99. Qin J, Zeng Y, Chen H, Tian J, Li Y. Permian sequence stratigraphy and sea–level changes in southwestern China. Lithofacies Paleogeography. 1998; 18(1):19–35.